UCLouvain

École polytechnique de Louvain

An improved thermodynamic model for supersonic ejectors

Author: **Antoine METSUE**
Supervisor: **Yann BARTOSIEWICZ**
Readers: **Philippe CHATELAIN, Romain DEBROEYER, Matthieu DUPONCHEEL**
Academic year 2019–2020
Master [120] in Mechanical Engineering

Abstract

Ejectors are passive devices that are used to suck and compress fluids. Their main advantage resides in the fact that they do not contain any moving parts, therefore limiting their required maintenance. They enable the use of low grade thermal energy sources, which makes their integration to refrigeration cycles especially compelling. The design process of such devices remains however particularly complex, and often requires expensive CFD or experimental investigation. So-called *thermodynamic* models are simple models that allow to swiftly predict ejector performance. Although such models are prominent in the literature, a general real gas model that could predict ejector performance for any set of operating conditions is still lacking.

In this thesis, a new real gas thermodynamic model is proposed. This model offers the possibility to evaluate ejector performance for on and off-design regimes, whether the flow is single-phase or two-phase, and taking friction losses into account. An emphasis has been set on the modeling of the choking phenomenology. In particular, the classical choking theory is compared to the compound-choking theory in the frame of ejector flows.

Acknowledgements

La rédaction de ce mémoire marque la fin d'une année riche en apprentissage, qui n'aurait pas pu être menée à bien sans le soutient de nombreuses personnes.

Je tiens premièrement à remercier mon promoteur, Yann Bartosiewicz, pour le temps qu'il a su m'accorder, pour son aide, ses conseils, ses relectures et surtout pour m'avoir poussé à fournir le meilleur de moi-même.

Je tiens aussi à remercier tout particulièrement Romain, pour avoir su m'aiguiller au cours de cette année, pour son temps, son aide et ses relectures.

Je souhaite également remercier toute l'équipe technique qui m'aura aidé tout au long de l'année et ce avec le sourire, même si la plupart des résultats expérimentaux n'auront finalement pas pu être obtenus. Un grand merci à Frank, Julien, Lily et Arnaud.

Je remercie aussi l'équipe d'Atelier François, Grégoire et Pascal, pour m'avoir aidé et supervisé lors de mes travaux expérimentaux.

Un grand merci dernièrement à ma famille, qui a su me supporter durant cette épreuve, ainsi qu'à mes amis qui ont pu me redonner du courage lors des périodes difficiles.

Contents

List of Figures

Nomenclature

A	Area	[m^2]
D	Diameter	[m]
G	Mass flux per unit area	[$kg/m^2/s$]
M	Mach number	[-]
R	Specific gas constant	[J/kg/K]
T	Temperature	[K]
V	Velocity	[m/s]
$\dot{m}$	Mass flow rate	[kg/s]
a	Speed of sound	[m/s]
h	Specific enthalpy	[J/kg]
p	Pressure	[Pa]
q	Quality	[-]
s	Specific entropy	[J/kg/K]
x	Horizontal coordinate	[m]

Greek letters

α	Compound-wave speed	[m/s]
β	Compound-flow indicator	[m^2]
ϵ	Error tolerance	[-]
η	Efficiency	[-]

γ	Heat capacity ratio	[-]
ω	Entrainment ratio	[-]
ψ	Constant mixing efficiency	[-]
ρ	Density	[kg/m^3]

Subscripts

0	Stagnation conditions
2	Diffuser inlet
c	Setpoint back pressure
d	Diffuser outlet
e	Primary nozzle exit
exp	Experiment
f	Fitting
$guess$	Guessed value
is	Isentropic conditions
m	Mixed flow
max	Maximum
mod	Model
N	Normal shock
out	Outlet conditions
p	Primary flow
PG	Perfect gas
RG	Real gas
s	Secondary flow
sat	Saturated vapour conditions
t	Primary throat
y	Hypothetical throat

Superscripts

$*$	Critical conditions

Abbreviations

CAM	Constant Area Mixing
CPM	Constant Pressure Mixing
HEM	Homogeneous Equilibrium Model
NXP	Nozzle Exit Position

CHAPTER 1

Introduction

1.1 Context

Ejectors are devices used to suck and compress fluids. In that way, their effect on the fluid is similar to that of a pump. Their applications are wide : in the aerospace industry for the making of high efficiency-high thrust engines [34], as steam ejectors for desalination applications [26], or to improve the efficiency of thermal power plants by recovering some of the wasted energy [21]. The use of ejectors is also of a particular interest for refrigeration systems because they offer the possibility to use low grade thermal energy sources, such as solar radiation or waste heat from industries, instead of electricity [4].

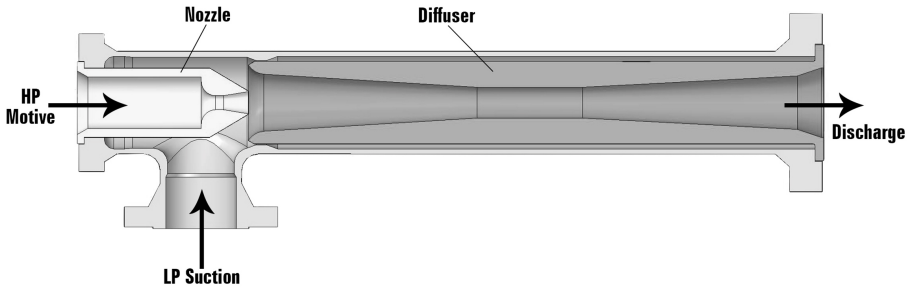

Figure 1.1: Diagram of a typical ejector [1].

As can be seen on the above diagram, ejectors have no moving parts, hence they are relatively low cost, need low maintenance, and they can work with a variety of fluids. The key principle is that a motive fluid – at high stagnation pressure – will discharge into a primary nozzle, and by doing so, will drive a secondary fluid – at low stagnation pressure – into a suction nozzle by Ventury effect. Primary and secondary fluids will then enter a secondary nozzle, called *mixing chamber*, and end up at the end of the diffuser with an

intermediate stagnation pressure.

Much as they may offer a compelling alternative to traditional compression devices, ejectors are nonetheless characterised by complicated fluid dynamics, and some of the mechanisms at play within the ejector remain insufficiently understood, which hinders the performance of the global system [8]. Though the most straightforward approach to acquire data might be to preform experiments, such a strategy would not be economically advantageous as it would require too much time and material resources [12]. Instead, numerical methods seem to be the most profitable way to generate results. To this end, three main approaches are commonly considered : Computational Fluid Dynamic (*CFD*), 1-D methods and thermodynamic methods [6].

Whilst CFD requires expensive computational resources, 1-D methods are simpler but nonetheless call for complex solving schemes [6]. The advantage of so-called *thermodynamic* or *0-D* methods thus lies in the fact that they can produce satisfactory results quite swiftly, which is why they are the most accounted for methods in the literature [6].

Likewise, a better understanding of the flow structure within the ejector may lead to more adequate models. The flow structure can be studied with CFD or through visualization techniques such as shadowgraphy or schlieren imagery [24]. Such experimental results are besides of great importance for the validation stage of numerical results.

1.2 Ejector Fundamentals

As stated in the previous section, the main advantage of an ejector is that it includes no rotating parts. It is composed of four main components : the primary nozzle, the suction chamber, the mixing duct (also referred to as the *mixing chamber*), and the diffuser. A secondary nozzle is formed by the whole assembly. An ejector has a threefold effect, specifically, pressure lift, mixing and entrainment [8]. Within the ejector, a high stagnation pressure fluid is mixed with a low stagnation pressure fluid, to end up with an intermediate pressure, referred to as *back pressure*, at the discharge. The high stagnation pressure stream is referred to in the literature as the *primary* – or *motive* – stream and is discharged through the *primary nozzle*, whilst the low pressure stream is referred to as the *secondary* – or *suction* – stream and is drawn into the *secondary inlet* [24]. Those will be identified, respectively, with indices p and s in the present document.

Ejectors can be classified according to their internal flow properties or according to their geometry. Those devices can work with two-phase or single phase flows, at subsonic or supersonic regimes, have different shapes and have one or more primary nozzles. In any

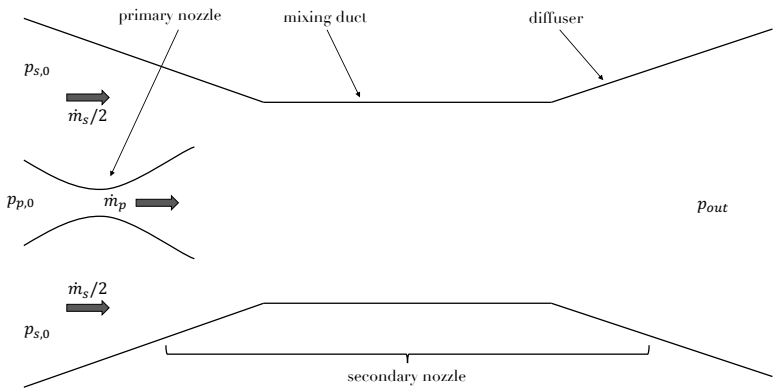

Figure 1.2: Schematic of an ejector.

case, the prevalent type is the cylindrical single nozzle ejector, because of its simplicity [2]. Single phase gas-gas ejectors are generally used to recover waste heat and have been the most widely studied up until now, whereas liquid-liquid ejectors are commonly used like regular pumps. Two-phase liquid-vapour ejectors can be used as jet-pumps or as condensing devices (the vapour condenses within the ejector). However, the modeling of two-phase ejectors remains quite limited [3, 9].

In regard to the geometry, two main types of ejectors stand up in the literature : constant area mixing (*CAM*) and constant pressure mixing (*CPM*) ejectors. For the former, the primary nozzle exit section is located in the constant area part of the mixing duct, whereas for the latter, it lies within the converging part of the secondary nozzle. Even though CAM ejectors can produce higher mass flow rates, CPM ejectors are preferred in practice because they offer a greater stability over a wider range of back pressures [13, 36]. The nozzle exit position (*NXP*) then constitutes a prominent parameter of research to enhance ejector performance. On a broader level, the ejector internal geometry is intrinsically linked to the ejector performance [36].

In the case of a supersonic ejector, the primary stream is expanded in the primary nozzle and reaches sonic conditions in the near vicinity of the nozzle throat. The flow then expands in the diverging part of the nozzle to reach supersonic velocities, hence no information can travel upstream. The flow is consequently said to be *choked*, because the mass flow rate is independent of the downstream conditions. As the primary stream expands through the nozzle, its velocity increases and its static pressure decreases to reach values inferior to the secondary fluid stagnation pressure. The secondary fluid is then accelerated towards the low static pressure jet that is driven out of the primary nozzle exit.

Complex turbulent mixing phenomena then occur in the mixing chamber ; the primary stream transfers a part of its energy and momentum to the secondary stream through shear effect and suction into the low pressure jet [2, 23]. During this process, the flow goes through a normal or a series of oblique shock waves that interact with the shear layer, thus re-compressing the fluid [9]. Upon the diffuser, the now subsonic mixed fluid further decelerates. Hence, the pressure further increases until it matches the back-pressure at the discharge.

Because ejectors are used as entrainment devices, a convenient quantity to characterise their performance is their entrainment ratio $\omega = \dot{m}_s / \dot{m}_p$. To outline the different regimes of an ejector, it is convenient to draw its characteristic curve, which depicts the evolution of the entrainment ratio as a function of the back-pressure. Figure 1.3 depicts a typical ejector characteristic curve. Depending on the operating conditions – i.e. the secondary and outlet pressures – and on the internal geometry of the ejector, the secondary flow might become choked as well [2, 23]. As a results, below a certain value of the back-pressure, the secondary flow also becomes independent of the upstream conditions. This particular value of the back-pressure at which, given a particular stagnation pressure ratio $p_{p,0}/p_{s,0}$, the secondary flow becomes choked, is referred to as the *critical pressure* and will be designated by p^*_{out}. This phenomenon also implies that below p^*_{out}, the entrainment ratio becomes constant and the ejector is said to operate in *on-design* or *critical* mode. Above the critical pressure, the ejector is influenced by the back-pressure. When the latter is increased, a shock wave moves into the mixing chamber, interacting with the mixing and hindering the secondary mass flow. The ejector is then said to operate in *off-design* or

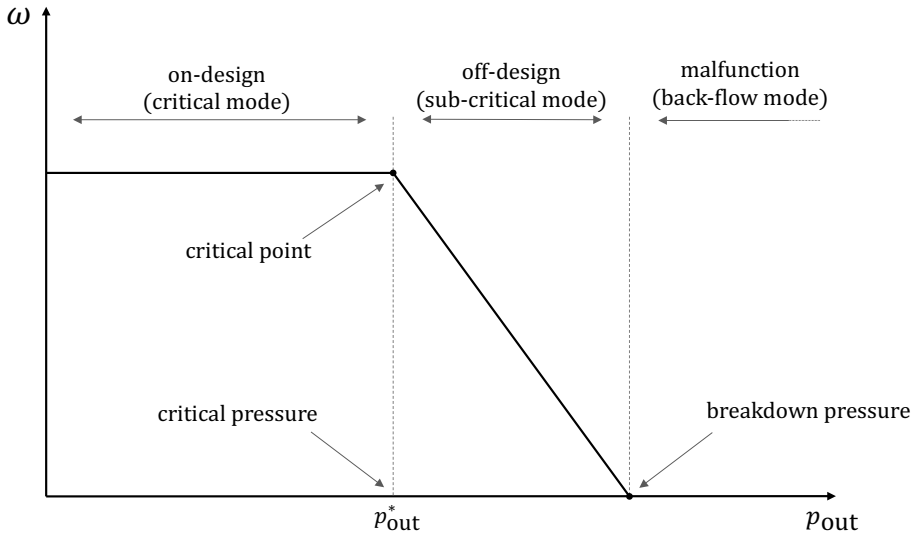

Figure 1.3: Characteristic curve of an ejector.

sub-critical mode. If the back-pressure is increased above a threshold value referred to as the *breakdown pressure*, the primary flow reverses back into the suction chamber [9]. This case corresponds to a malfunction of the ejector.

1.3 Internal flow structure

The flow regimes taking place inside of a supersonic nozzle are well described by aerodynamics of internal flows [10]. Three different flow structures may be encountered and are depicted in Figure 1.4 [2, 10]:

- The jet reaches supersonic conditions, but cannot sustain it through the entirety of the divergent section because the inlet pressure is not high enough. A normal shock is induced in the divergent and the flow exits the nozzle at subsonic speed. The flow is said to be *unprimed*.
- If the inlet pressure is increased, the flow will exit the nozzle at supersonic speed, but will go through a series of oblique shocks if the exit pressure is lower than the ambient pressure. Consequently, the flow is said to be *over-expanded*.
- If the inlet pressure is further increased, the exit pressure of the nozzle becomes higher than the ambient pressure. The jet will further expand through expansion waves. The flow is then said to be *under-expanded*.

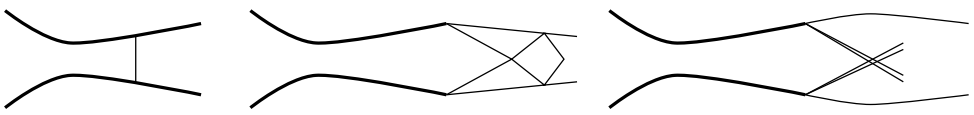

Figure 1.4: Flow regimes within a nozzle : (a) unprimed nozzle flow; (b) over-expanded flow; (c) under-expanded flow [10].

Although the flow structure within a nozzle is well described, the mixing processes at play within an ejector are complex and remain to this day not fully understood [23]. An improved knowledge of the relations between the internal flow structure and the operating parameters and geometry of the ejector is required to enhance their design methodology and therefore improve the performance of the global system they are part of. Though a clear link between operation and flow structure is sill lacking, several flow regimes have been observed and are sketched in Figure 1.5 [17, 27] :

- Fully supersonic flow : the primary jet fully expands in the mixing chamber and the entrained secondary flow becomes supersonic. This regime is observed for high values of motive pressure and small induced secondary flows.

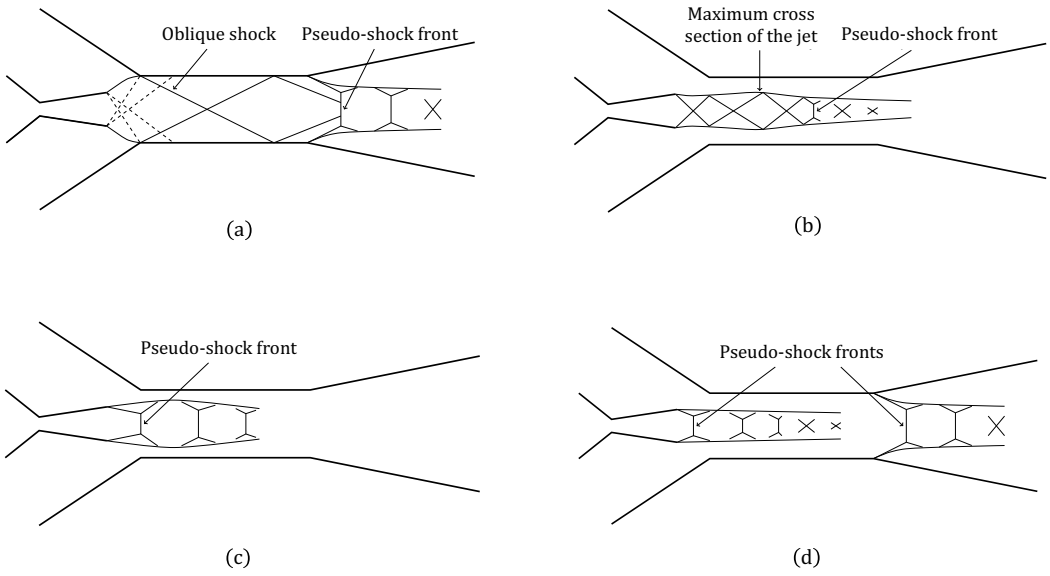

Figure 1.5: Flow regimes within an ejector : (a) fully supersonic flow; (b) choked secondary flow; (c) shock-between-throats flow; (d) doubly choked flow [10].

- Choked secondary flow : the expansion of the primary jet is lesser than for the fully supersonic flow. Hence, the secondary mass flow rate gets higher. For small entrainment ratios, the secondary flow chokes in the secondary nozzle, i.e. before the mixing chamber inlet. As the entrainment ratio gets higher, the choking section gets closer to the mixing chamber until the latter is reached. Then, there is a particular section located inside of the mixing chamber at which the secondary flow reaches sonic velocities. Beyond the choking section, the secondary flow is further expanded and both primary and secondary flows are supersonic. If the primary nozzle is unprimed, this regime is also called *mixed flow with separation*.

- Shock-between-throats flow : if the primary pressure gets relatively low, the oblique shock waves in the primary jet will move towards the primary nozzle and a pseudo-shock will form at the exit of the primary nozzle. The secondary flow is induced by a subsonic primary flow ; it is thus also subsonic. The induced mass flow rate is limited by the back-pressure.

- Doubly choked flow : the flow is choked both at the primary nozzle throat and at the ejector throat (i.e. the constant area duct). Both primary and secondary flows are sonic in the constant area part of the mixing chamber. This regime is observed for small mixing chamber areas. Two pseudo-chocks can be observed : the first one at the primary nozzle exit and the second one at the diffuser inlet.

1.4 Mathematical modeling

This section constitutes a brief state of the art of the thermodynamic modeling of supersonic ejectors. The emphasis will be set on constant pressure mixing models, as they constitute a sizable part of the material for the following chapters.

1.4.1 Single-phase models

The first one-dimensional mathematical model of an ejector was introduced by Keenan et al. [22] in 1950. The model was based on the application of mass, momentum and energy conservation equations, with the use of isentropic flow relations. This model has been used as a theoretical basis in ejector design since then [30].

However, the model of Keenan et al. [22] assumed that both primary and secondary streams had the same pressure at the primary nozzle exit section, and began to mix at that location. As a result, this model was unable to provide information on the choking phenomena at play within a supersonic ejector [19].

Munday and Bagster [28] later proposed modifications to the model of Keenan et al. [22]. Their theory assumed that the two streams did not mix right away at the exit of the primary nozzle, but they rather conserved their integrity up until a particular downstream section. It was postulated that an hypothetical throat was formed by the primary flow and the ejector wall and that the secondary stream reached sonic velocity at that particular location (cfr. Figure 1.6). The two streams then mix at constant pressure. This phenomenology is somewhat related to the *chocked secondary flow* pattern that was discovered experimentally by Fabri and Siestrunck [17] in 1958. Since the presence of an hypothetical throat constitutes the basis of numerous mathematical models, the choking mechanism associated with this regime is often referred to as *Fabri-choking* [23, 24].

In 1995, Eames et al. [16] introduced a model that included irreversibilities due to friction losses inside of the primary nozzle, mixing chamber and diffuser with the use of isentropic efficiencies. Their model was also based on the constant pressure mixing theory, but unlike Munday and Bagster [28], they did not impose the choking of the secondary flow. Based on the work of Eames et al. [16] and with the hypothesis of perfect gas, Aly et al. [5] implemented a few years later a computer code to compute the pressure and Mach number of the flow in the ejector.

In order to take into account the choking of the secondary flow, Huang et al. [20] introduced a new model of double-choking that took irreversibilities into account, but for

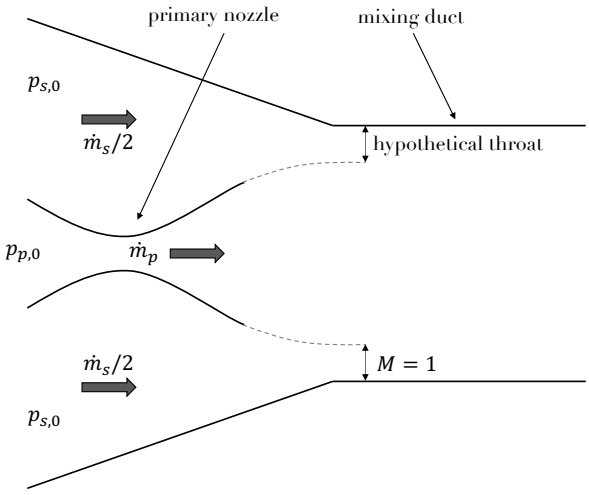

Figure 1.6: Schematic diagram of the Fabri-choking mechanism.

which they considered that the mixing phenomena occurred inside of the constant area duct. The secondary flow then reaches sonic conditions at the location of an hypothetical throat, like postulated by the theory of Munday and Bagster [28]. To validate their model, they carried out experiments for 11 different ejector geometries, using R141b as working fluid. The experimental results were used to determine the efficiency/loss coefficients defined in their 1-D model. It is to note that since the models of Eames et al. [16] and Huang et al. [20] both considered that the mixing occurs in the constant area duct, their models can be considered as both CPM and CAM models.

Nonetheless, all previous models are based on the hypothesis of perfect gas. Rogdakis and Alexis [31] solved that problem by using this time real gas thermodynamic properties with real gas – general – conservation equations. The friction losses were taken into account with the use of constant isentropic efficiencies. Yet, the friction losses are closely related to the velocities, and the latter can vary quite a lot along the ejector [19]. Selvaraju and Mani [32] then developed a real gas model based on Munday and Bagster's [28] choking theory but taking into account frictional losses inside the mixing chamber, using this time a turbulent friction factor depending on the Reynolds number of the mixed flow.

However, previous 1-D models could only predict ejector performance at critical mode operation. In 2013, Chen et al. [11] introduced a model to predict ejector performance at critical and sub-critical operational regimes. Their CPM model is also based on the presence of an hypothetical throat inside of the constant area duct. For the sub-critical operating regime, this hypothesis was conserved. The off-design performance was ob-

tained by using a mixing efficiency dependant on the back-pressure of the ejector. Perfect gas behaviour was assumed and isentropic efficiencies were used to take friction losses into account. A few years later, Chen submitted a modified version of the model, allowing this time the use of real gas thermodynamic properties [12].

1.4.2 Two-phase models

The preceding models all relied on single phase compressible flows and the fact that the pressure might be recovered with a normal shock. However, in applications such as refrigeration cycles, phase change can occur, leading to a condensation shock [19]. In 1998, Sherif et al. [33] presented an isentropic homogeneous expansion/compression model that allowed phase change. In their model, they considered an ejector whose primary fluid was a two-phase mixture and whose secondary fluid was either a subcooled or saturated liquid with the same chemical composition as the primary fluid. The main difference with single phase models was the introduction of the quality of the fluid in the computation of the density, enthalpy and entropy [19].

While the model of Sherif et al. [33] allowed to determine the thermodynamic states at each section of the ejector, it required to input the entrainment ratio. In 2005, Cizungu et al. [14] proposed a thermodynamic model to describe and optimize single and two-phase ejectors. This time, assuming constant pressure mixing, the entrainment ratio could be computed on the basis of operating and geometrical parameters. Furthermore, a method for computing the optimum geometry of the ejector was proposed.

In 2014, Ameur et Al. [6] proposed a modeling procedure for on-design liquid-vapour ejectors. As pointed out in the article, the speed of sound in a fluid with phase change is difficult to determine accurately, especially when the phases exhibit large velocity and temperature differences. Therefore, primary and secondary flows are computed in such a way as to maximise the mass flow rate, without the need to impose unity Mach number at the throat. Real gas thermodynamic fluid properties were this time obtained with the use of tabulated data.

Taslimi et al. [35] later developed a new thermodynamic model, this time for both single choking and double choking conditions. Unlike in previous work, the irreversibilities due to friction are taken into account using polytropic efficiencies, instead of isentropic efficiencies. Moreover, a method for the computation of ejector dimensions under on-design operating conditions is proposed. The model relies on an homogeneous equilibrium model (HEM), meaning that it was assumed that the velocity, pressure and temperature of the two phases are equal. This hypothesis was also used by Ameur et al. [6], though

only for investigation on the Mach number.

1.4.3 Choking mechanism

As pointed out by Lamberts et al. [24], a thorough investigation regarding the secondary stream choking phenomenology within supersonic ejectors has not yet been proposed in the literature. In fact, the *Fabri-choking* is used as the foundation of most thermodynamic ejector models [25], including all of the aforementioned models ([6, 12, 14, 16, 20, 28, 31, 32, 33, 35]). However, the Fabri-choking has only been experimentally observed once, in the study of Lamberts et al. [24]. Indeed, according to the authors, in many works where on-design ejectors are studied, no apparent sonic section in the core of the secondary stream is observed. Hence, the *Fabri-choking* is not necessarily representative of the actual phenomena occurring inside of a doubly choked ejector.

In his article, Lamberts et al. [25] describes a new choking theory based on the early work of Bernstein et al. [7] about the so-called *compound-choking* theory. This choking mechanism, as opposed to the classical *Fabri-choking* mechanism, does not impose unity Mach number at the hypothetical throat of the ejector, but states that the choking rather occurs when the secondary stream reaches a certain Mach number inferior to one. It was found that the model generally provided better results compared to more complex 1-D models for on-design operation [25].

1.5 Scope of this study

As illustrated in the previous sections, off design thermodynamic models are still limited. More precisely, a 0-D model that could predict ejector performance for all operating regimes and for both single and two-phase flows is still lacking. Furthermore, with the exception of the model of Lamberts et al. [25], all previously cited models are based on the hypothesis that the Fabri-choking mechanism is the correct choking phenomenology for ejector flows.

The purpose of the present work is therefore to propose a new thermodynamic model for on and off-design operation, based on the use of real gas thermodynamic properties. The goal is to develop a model that allows predictions for both single and two-phase flows, taking friction irreversibilities into account, and that is not limited to the use of the classical choking criterion (i.e. the Fabri-choking criterion). Therefore, one feature of the model should be the ability for the user to choose the choking criterion – Fabri-choking or compound-choking – to be used for predictions.

The core of the present document is divided in three main chapters :

- **Chapter 2**
  Chapter 2 is divided in two main sections. First, the main assumptions used to derive the model will be presented along with the model layout. The model of Chen et al. [12] will be used as a basis to construct the on-design part of the thermodynamic model. The choking conditions for the primary flow will be found by maximising the primary mass flow rate. This latter approach will be discussed. Then, the two aforementioned choking criteria will be mathematically derived. An emphasis will be set on the derivation of the compound-compressible nozzle flow theory of Bernstein et al. [7]. This will lead to the implementation of an alternative computation method for the speed of sound, required to avoid potential issues with two-phase flows.

  The second part of chapter 2 will be dedicated to the application of the on-design model on the eleven ejector geometries of Huang et al. [20]. Both choking criteria will be compared to the experimental data. The implementation of the compound-choking criterion will also be validated against the perfect gas model of Lamberts et al. [25].

- **Chapter 3**
  In this chapter, the off-design part of the thermodynamic model will be developed. Once again, the model of Chen et al. [12] will constitute the basis upon which the present model will be developed. Some alterations will be made, which will lead to the implementation of a new off-design model. This latter model will be discussed and a thorough comparison of the two choking mechanisms will be performed. This will shed light on the connections between Fabri-choking and compound-choking.

- **Chapter 4**
  This chapter will be devoted to the calibration of the new 0-D model with experimental data found in the literature. First, the individual impact of each calibration parameter will be investigated. Then, the model will be calibrated on the experimental data gathered by Garcia del Valle et al. [15], and compared after calibration to the data obtained for the three ejectors of Hakkaki-Fard et al. [18]. In a second step, the model will be calibrated with the experimental data obtained from the air ejector available at UCLouvain. Lastly, the impact of friction losses on the compound-choking criterion will be discussed.

CHAPTER 2

On-design thermodynamic model

2.1 Introduction

As detailed in the state of the art in the first section of the present document, numerous 0-D or so-called *thermodynamic* models can be found in the literature. The model of Chen et al. [12] will be used as a basis for the present research, with some alterations. As a reminder, this model is able to estimate the performance of an ejector on overall modes. It uses real gas thermodynamic properties given by the `REFPROP` Python library. It is to note that the thermodynamic properties that will be used for the present work will be computed by the use of the tabulated data provided by the `COOLPROP` Python library. This choice is mainly motivated by the fact that, unlike `REFPROP`, `COOLPROP` is free. It is now proposed to review the model that was implemented, starting in this chapter with the on-design operation. The differences with the initial model of Chen et al. [12] will be highlighted.

2.2 Model layout

As stated previously, the flow within an ejector is quite complex and thus often requires the use of assumptions in order to solve the flow swiftly, which is the purpose of thermodynamic models. The main assumptions used for the present work are :

1. The flow is one dimensional, steady and adiabatic. The inlet (primary and secondary), as well as the outlet velocities, are negligible.

2. Friction losses due to the wall and the shear layer between the primary and secondary flows are taken into account by the use of several isentropic efficiencies : η_p for friction within the primary nozzle, $\eta_{p,y}$ for friction losses undertaken by the primary flow within the mixing chamber and η_s for friction losses undertaken by

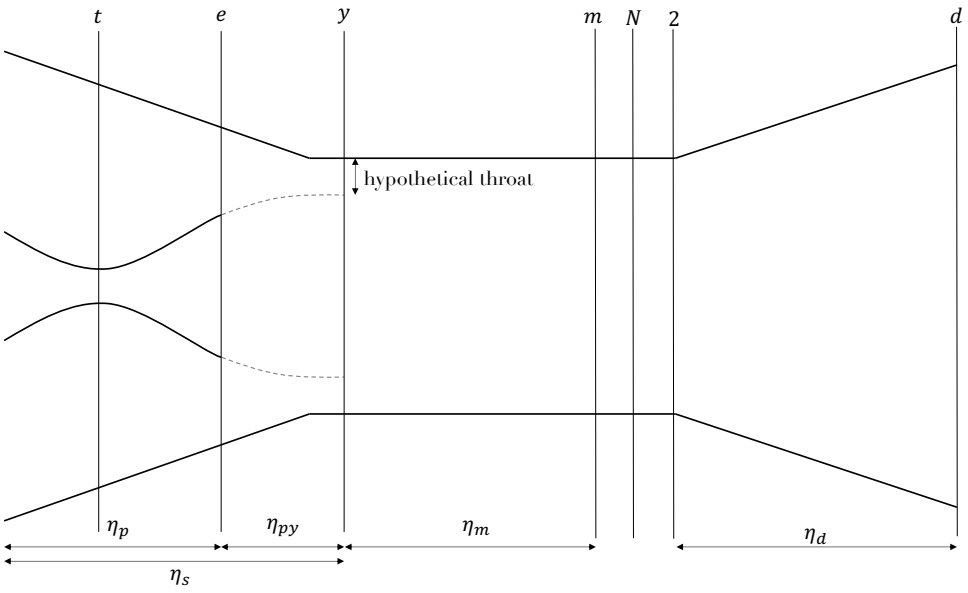

Figure 2.1: Schematic diagram of the model.

the secondary flow within the mixing chamber. The mixing losses between primary and secondary flows are taken into account by means of a loss coefficient η_m (cfr. Figure 2.1).

3. Real gas properties will be retrieved from the tabulated data provided by `COOLPROP`.

4. Primary and secondary flows do not start mixing up until a particular section – that will be referred to as *mixing section* – located inside of the constant area duct. At that location, both pressures are assumed to be equal and the mixing process takes place at a constant pressure equal to the one at said mixing section. The location of the particular section at which the mixing phenomena begin is the location of the hypothetical throat that is well described in the literature.

A schematic of the ejector, along with the notations that will be used in what follows, is shown in Figure 2.1. Since the primary flow is assumed to be choked, the primary mass flow rate $\dot{m}_p$ is constant and does not depend on any downstream quantity (i.e. it only depends on primary stagnation conditions). The primary flow expands in the primary nozzle, and than further more in the mixing chamber until it reaches section y. The secondary flow is also expanded upon section y, and then only the mixing process starts. In other words, the two flows are essentially independent up until reaching section y. It is important to note that the position of the mixing section y is assumed to lie within the constant area section, weather or not the ejector is working in on or off-design.

Then, the two flows start to mix at constant pressure, and are assumed to be completely mixed upon section m. If the flow is supersonic at section m, it consequently goes through a normal shock at section N, located in the constant area section as well. The flow thus reaches the diffuser inlet – section 2 – at a subsonic speed. It then further expands in the diffuser, where the flow velocity is further decreased and the pressure recovered.

2.3 Primary nozzle

The flow in the primary nozzle can be solved from the knowledge of the stagnation conditions, along with the knowledge of the isentropic efficiency that governs the flow in this part. It is convenient to set the stagnation conditions with the primary pressure $p_{p,0}$ and the primary temperature $T_{p,0}$. When working with saturated fluids, it is sometimes convenient to define stagnation conditions with the quality of the fluid $q_{p,0}$. For the sake of simplicity, the stagnation conditions will be defined with $p_{p,0}$ and $T_{p,0}$ in what follows.

First, the enthalpy and entropy of the primary flow at the inlet can be computed from the pressure and temperature :

$$h_{p,0} = h(p_{p,0}, T_{p,0}), \tag{2.1}$$

$$s_{p,0} = s(p_{p,0}, T_{p,0}). \tag{2.2}$$

For a given pressure p_p and assuming an isentropic expansion, the enthalpy at said pressure can be computed :

$$h_{p,is} = h(p_p, s_{p,0}). \tag{2.3}$$

With knowledge of the isentropic efficiency of the primary nozzle η_p, one can then compute the enthalpy resulting from the non-isentropic expansion process:

$$h_p = h_{p,0} - \eta_p \, (h_{p,0} - h_{p,is}). \tag{2.4}$$

The density along the expansion can then be computed from the knowledge of pressure and enthalpy, and from the conservation of total enthalpy, one can then compute the flow velocity :

$$\rho_p = \rho(p_p, h_p), \tag{2.5}$$

$$V_p = \sqrt{2 \, (h_{p,0} - h_p)}. \tag{2.6}$$

The hypothesis of choked primary flow has then to be used in order to solve the flow. The classical way to impose such a condition, is to impose Mach unity at the nozzle throat. Although this is the approach taken in the model of Chen et al. [12], it was chosen to impose the choking condition by maximisation of the mass flow rate. This approach presents two advantages. First, one does not require to know the speed of sound at the throat for the computation of the primary mass flow rate, which can sometimes be problematic for two-phase flows as the `COOLPROP` library is flawed for thermodynamic conditions close to the saturation curve. Then, if one considers a non-isentropic flow, the sonic section is not actually located at the geometric throat of the nozzle, but rather at a certain distance downstream. Imposing Mach unity at the throat would consequently lead to an error in the computation of the primary mass flow rate. By rather directly maximising the mass flow rate, this problem is avoided. Furthermore, in the case of an isentropic nozzle flow, it can be shown that maximising the mass flow rate per unit area is equivalent to imposing Mach unity at the throat. This result is demonstrated in Appendix A.1.

The mass flux per unit area is defined as :

$$G = \rho V. \tag{2.7}$$

From Equations 2.1 through 2.7, the expansion of the fluid in the primary nozzle can be

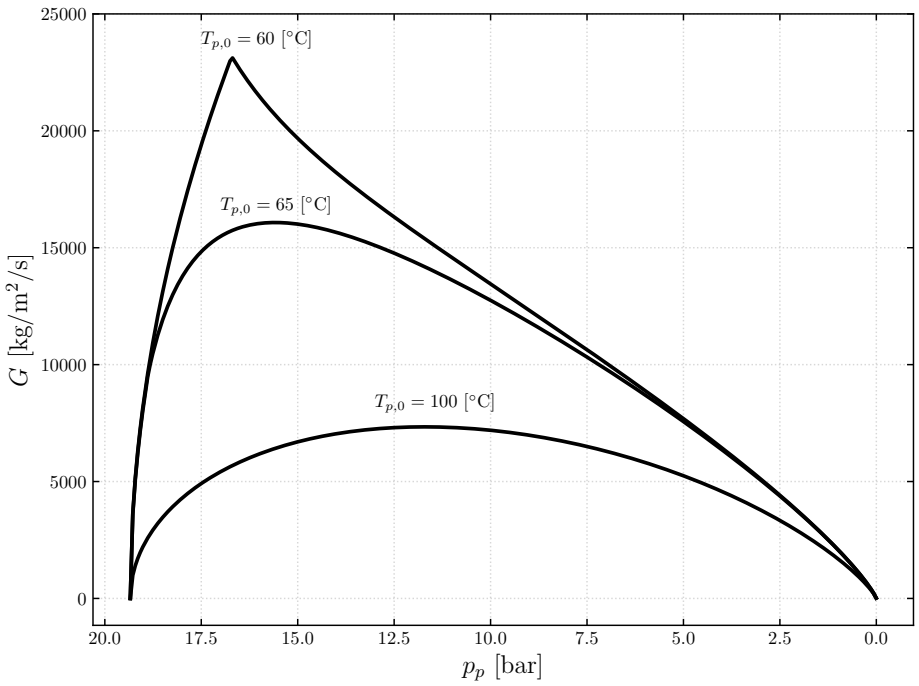

Figure 2.2: Mass flux per unit area for different stagnation temperatures for R134a, $p_{p,0}$ = 1.934 [MPa] and $\eta_p = 0.97$.

computed. Figure 2.2 shows the typical behavior of G along an expansion with R134a as working fluid, and Figure 2.3 shows the expansion path in a T-S diagram, for various stagnation conditions.

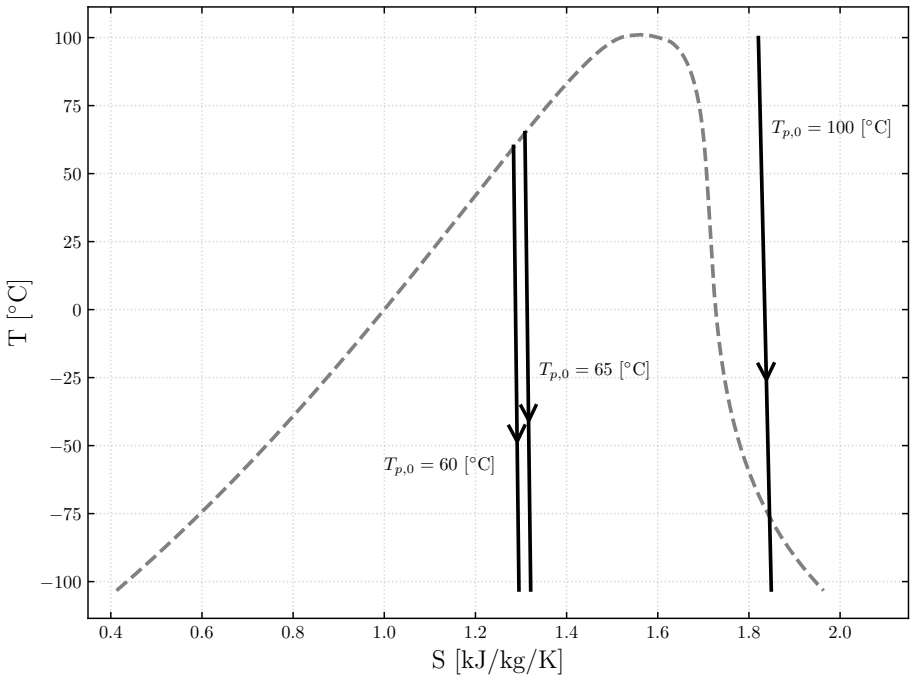

Figure 2.3: Expansion paths for the three expansions shown in Figure 2.2. The dashed grey curve corresponds to the saturated liquid and saturated vapour curves.

One can observe that the mass flow rate per unit area has a maximum along the expansion. Furthermore, this maximum gets higher and closer to the stagnation pressure as the stagnation temperature gets lower, i.e. the stagnation conditions get to the left hand side of the saturation curve. Indeed, as the temperature gets lower, the fluid transitions from a superheated vapour (for $T_{p,0} = 100°C$) to a denser subcooled liquid. The much higher density of a liquid explains why the maximum of G gets higher. In addition, as $T_{p,0}$ gets lower, the isobars get closer to the saturated liquid curve, therefore shifting the maximum of G to the left (i.e. at a pressure closer to the stagnation pressure) because the maximum mass flow rate is achieved near the region where the flow is the most dense, that is, at the saturation curve.

For stagnation conditions where the fluid is highly subcooled, there is actually an angular point at the location of the maximum, as the fluid flashes along the expansion. By doing so, the fluid looses a great deal of density in an almost discontinuous fashion. This brings forward the need to compute very accurately the position of the maximum, because due to this angular point, a slight imprecision will lead to a substantial error in the mass flow

rate. To compute efficiently the maximum mass flux, it is convenient to use the fact that G has only one maximum. Therefore, one can proceed iteratively by computing $G = f(p_p)$ for a reduced amount of linearly spaced points, and then narrowing the interval on p_p where the maximum is located until finding the solution with the desired precision.

With knowledge of the maximum mass flow rate per unit area $G_{p,max}$ and the throat area of the nozzle A_t, the mass flow rate for the choked primary nozzle is found by :

$$\dot{m}_p = G_{p,max} A_{p,t}. \tag{2.8}$$

The throat thermodynamic state is then fully solved, as G_{max} provides the knowledge of the throat pressure p_t, which can later be used to find the throat enthalpy h_t by the use of Equations 2.3 and 2.4. The velocity at the throat is then found using Equation 2.6.

It is important to note that the `COOLPROP` library is faulty near the critical point, meaning that requesting the computation of a thermodynamic quantity near said region generates an error. In order to circumvent this issue and prevent the whole operation to stop, it was chosen to manage this error by assuming that the thermodynamic quantities near the vicinity of the faulty region are equal to the quantities slightly above or slightly below the critical point. Except in the rare case where the maximum of G is located exactly at the critical point, this maneuver does not lead to any loss of precision.

The nozzle exit conditions are found by further expanding the flow from the known state at the throat. Knowing the exit section area $A_{p,e}$, the exit state of the fluid is found by using the mass and total enthalpy conservation equations. Indeed, the flow must satisfy :

$$V_{p,e} = \frac{\dot{m}_p}{\rho_p A_{p,e}} \tag{2.9}$$

and

$$V_{p,e} = \sqrt{2(h_{p,t} - h_p) + V_{p,t}^2}\ , \tag{2.10}$$

where h_p and ρ_p can be computed along the expansion (i.e. as a function of p_p) in the divergent of the nozzle with the use of Equations 2.4 and 2.5, respectively. The solution $V_{p,e}$ is found by selecting the unique value that allows Equations 2.9 and 2.10 to be satisfied simultaneously. Once again, the state at the primary nozzle exit is then fully defined, as the value of $V_{p,e}$ provides direct knowledge of ρ_p and h_p.

2.4 Mixing chamber

The mixing chamber is the part of the ejector where the primary and secondary flows will come into contact. The secondary flow is solved using the same computation algorithm as for the primary flow, with the exception that one only has to solve the secondary flow up to the throat, that is, the hypothetical throat of the ejector. However, the area of said hypothetical throat is unknown, and the primary and secondary flows in the mixing chamber thus have to be solved simultaneously. It is proposed to first consider the case where the ejector is working under critical regime. In this scenario, the ejector performance only depends on the flow behaviour up to the hypothetical throat. Indeed, since the ejector itself is choked, information cannot travel upstream. Note that the computation of the critical back pressure will be derived in the next chapter.

The present work focuses on two different approaches to the choking phenomenon within an ejector. First, the *classical* choking criterion, which states that the ejector is choked if both primary and secondary flows are choked. This choking criterion is referred to as *Fabri-choking*. The most common way to impose this criterion is to simply impose Mach unity at the throat. As explained previously, it was rather chosen here to maximise the mass flow rate, which can be viewed as an improved Fabri-choking criterion. The second choking criterion is the *compound-choking* criterion, which states that the ejector is choked when primary and secondary flows reach particular Mach numbers not equal to unity ; the Mach number of the primary flow is superior to one and that of the secondary flow is inferior to one. In this section, it is proposed to review the flow solving algorithm for both choking criteria.

2.4.1 Fabri-choking

When using the *Fabri-choking* criterion, one maximises the primary and secondary mass flow rates separately. It is nevertheless necessary to solve both flows simultaneously. As stated above, the hypothetical throat area is unknown, but it is still possible to compute G_{max} for the secondary flow. This is done in the exact same fashion as for the primary flow, using Equations 2.1 through 2.7, except that the isentropic efficiency and the stagnation conditions correspond to the ones of the secondary flow.

Once again, the knowledge of $G_{s,max}$ directly provides the knowledge of the thermodynamic state at the hypothetical throat (i.e. $p_{s,y}$, $h_{s,y}$). Since it is assumed that the pressure at the aerodynamic throat is equal for both streams, one has that :

$$p_{p,y} = p_{s,y}. \tag{2.11}$$

Hence, the expansion of the secondary flow provides information on how much the primary flow has to expand from the nozzle exit to reach the required pressure for the secondary flow to be choked as well. Since the pressure at the end of the expansion is known, along with the isentropic efficiency taking into account the friction losses undertaken by the primary flow between sections e and y, it is straightforward to find the other quantities governing the primary flow at section y. First, the enthalpy of the primary flow at section y is retrieved :

$$h_{p,y,is} = h(p_{p,y}, s_{p,e}). \tag{2.12}$$

The isentropic efficiency $\eta_{p,y}$ is then used to correct the enthalpy value :

$$h_{p,y} = h_{p,e} - \eta_{p,y}\,(h_{p,e} - h_{p,y,is}). \tag{2.13}$$

The density of the primary flow is found by :

$$\rho_{p,y} = \rho(p_{p,y}, h_{p,y}). \tag{2.14}$$

The total enthalpy and mass conservation equations are subsequently used to compute $V_{p,y}$ and $A_{p,y}$:

$$V_{p,y} = \sqrt{2(h_{p,e} - h_{p,y}) + V_{p,e}^2}\ , \tag{2.15}$$

$$A_{p,y} = \frac{\dot{m}_p}{\rho_{p,y} V_{p,y}}. \tag{2.16}$$

Since it was assumed that the mixing section y is located inside of the constant area duct, it is possible to derive the secondary throat area $A_{s,y}$ from the knowledge of the total area of the duct A_y :

$$A_{s,y} = A_y - A_{p,y}. \tag{2.17}$$

The secondary mass flow rate is then computed :

$$\dot{m}_s = G_{s,max}\ A_{s,y}. \tag{2.18}$$

The on-design entrainment ratio is finally obtained as the ratio between secondary and primary mass fluxes :

$$\omega = \frac{\dot{m}_s}{\dot{m}_p}. \tag{2.19}$$

Figure 2.4 shows the flowchart of the computation algorithm that was described in this section.

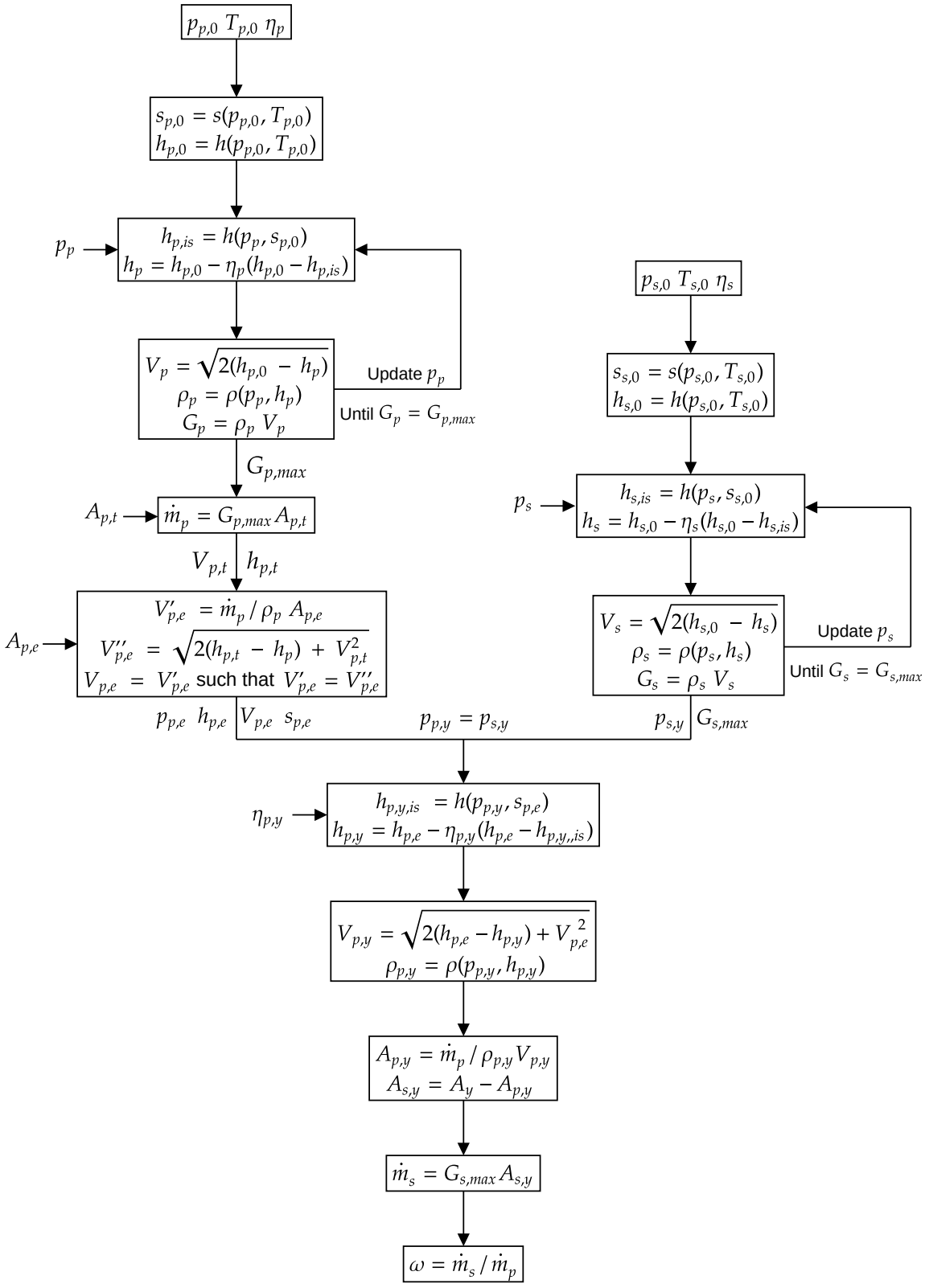

Figure 2.4: Flowchart of the model for on-design operation using the Fabri-choking criterion (cfr. Figure 2.1). Note that the computation of the critical back pressure will be performed in the following chapter.

2.4.2 Compound-choking theory

When using the *compound-choking* criterion, one maximises the primary and secondary mass flow rates together, as a whole. The compound-choking criterion derives from the compound-compressible nozzle flow theory that was first proposed by Bernstein et al. [7] for analyzing the behavior of one or more gas streams flowing through a single nozzle. In this section, it is proposed to review the fundamentals of the compound-compressible flow theory, and subsequently to apply it to ejector to define the compound-choking criterion.

Compound-compressible nozzle flow

Figure 2.5 shows a schematic of the compound-compressible flow model. The flow is represented as a series of sub-streams. At any position of the nozzle, one has :

$$A = \sum_{i=1}^{n} A_i \tag{2.20}$$

and

$$\frac{dA}{dx} = \sum_{i=1}^{n} \frac{dA_i}{dx}, \tag{2.21}$$

where A is the total cross sectional area, A_i is the flow area of the ith stream, and n is the number of streams that are considered.

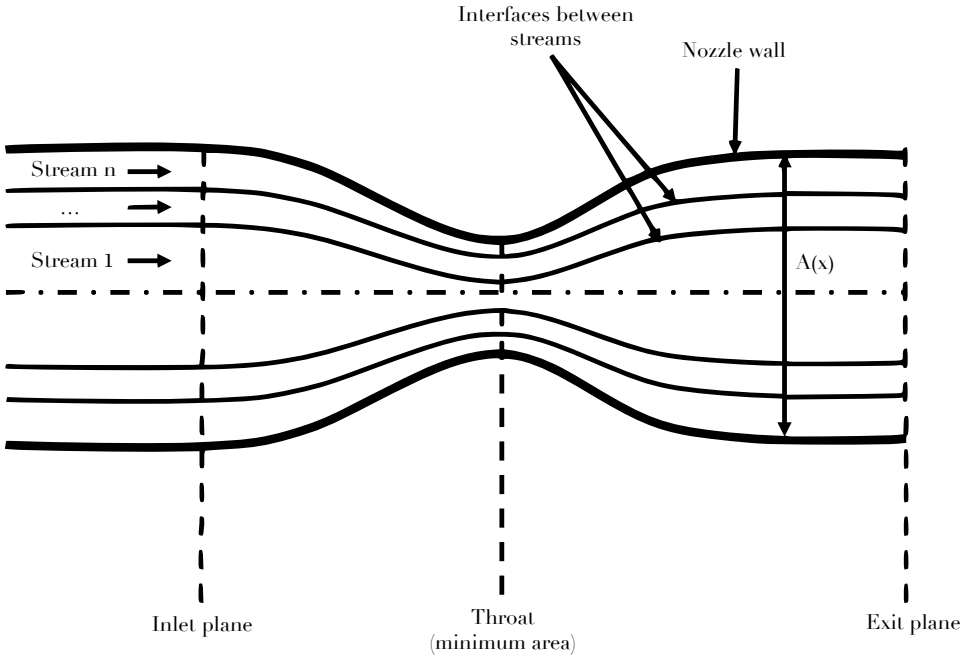

Figure 2.5: Schematic of the compound-compressible nozzle flow model.

The theory of Bernstein et al. [7] states that in order for the flow to be choked, one does not require for all sub-streams to reach sonic conditions at the throat. Choking rather occurs for particular conditions for which part of the streams reach supersonic velocities at the throat while others remain subsonic. In other terms, the information is propagated by means of a so-called *compound wave*. When this compound wave cannot travel upstream, the flow is choked.

The main assumptions of the compound-compressible flow theory are :

1. The flow is one dimensional, steady, adiabatic and isentropic.
2. There is no mixing between streams.
3. The pressure is constant between streams at each cross section.
4. The transverse pressure gradient caused by the streamline curvature is negligible.

In the original paper of Bernstein et al. [7], a compound-flow indicator β was proposed under the additional hypothesis that the fluid is a perfect gas with constant thermodynamic properties :

$$\beta = \sum_{i=1}^{n} \frac{A_i}{\gamma_i} \left(\frac{1}{M_i^2} - 1 \right), \tag{2.22}$$

where $\gamma_i = c_{p,i}/c_{v,i}$ is the heat capacity ratio and M_i is the Mach number of the ith stream. The indicator gives information about the compound flow regime, namely :

- $\beta > 0$: compound-subsonic flow.
- $\beta = 0$: compound-sonic flow.
- $\beta < 0$: compound-supersonic flow.

The compound-choking criterion is thus $\beta = 0$. However, Equation 2.22 is unusable for the purpose of this work, as it was chosen to suppress the hypothesis of perfect gas. It is nonetheless possible to extend the theory of Bernstein et al. [7] to provide an indicator for real gases. Using the hypothesis listed above, the mass conservation equation for each stream is given by :

$$\rho_i v_i A_i = \text{constant}, \tag{2.23}$$

which re-writes successively into :

$$\frac{d\rho_i}{\rho_i} + \frac{dV_i}{V_i} + \frac{dA_i}{A_i} = 0, \tag{2.24}$$

$$dV_i = -V_i \left(\frac{d\rho_i}{\rho_i} + \frac{dA_i}{A_i} \right). \tag{2.25}$$

Likewise, the momentum conservation equation reads :

$$\rho_i V_i A_i \, dV_i = -A_i \, dp_i. \tag{2.26}$$

Thirdly, since it was assumed here that the flow is isentropic, one can use the fact that

$$d\rho = \left(\frac{\partial \rho}{\partial p} \right)_s dp = \frac{1}{a^2} \, dp, \tag{2.27}$$

where a is the speed of sound. Using the definition of the Mach number $M = \frac{V}{a}$ and injecting Equations 2.25 and 2.27 into Equation 2.26, one obtains :

$$\frac{dA_i}{A_i} = \frac{dp}{\rho_i V_i^2} \left(1 - M_i^2 \right), \tag{2.28}$$

where the assumption of constant pressure along each section was used, such that $dp_i = dp$. Following the development of the theory in the original paper of Bernstein et al., the compound-flow indicator is defined as :

$$\frac{d}{dx} \left(\ln(p) \right) = \frac{1}{\beta} \, \frac{dA}{dx}. \tag{2.29}$$

Using Equation 2.21 and isolating β, the latter expression re-writes :

$$\beta = p \sum_{i=1}^{n} \frac{dA_i}{dp}. \tag{2.30}$$

From Equation 2.28, the generalisation of the compound-flow indicator to a real gas is therefore :

$$\beta = p \sum_{i=1}^{n} \frac{A_i}{\rho_i V_i^2} \left(1 - M_i^2 \right). \tag{2.31}$$

It is, at this point, relevant to address the issue of friction losses. Indeed, one of the hypothesis that were used to derive the present expression of β is that the flow is isentropic. However, the ejector model described previously takes friction into account by means of isentropic efficiencies ; the flow is not in all generality isentropic. This actually means that the compound-choking criterion $\beta = 0$, with β as expressed in Equation 2.31, is not rigorously correct if one considers non isentropic flows. It can be found that lifting the hypothesis of isentropic flow leads to the addition of two terms to the expression of β :

$$\beta = p \sum_{i=1}^{n} \frac{A_i}{\rho_i V_i^2} \left(1 - M_i^2 \right) - \frac{A_i}{\rho_i} \, \frac{\partial \rho_i}{\partial s_i} \Big|_p \, ds_i + F_i. \tag{2.32}$$

The second term of the right hand side in the latter equation comes from the fact that because the flow is non isentropic, Equation 2.27 becomes :

$$d\rho = \left(\frac{\partial \rho}{\partial p}\right)_s dp + \left(\frac{\partial \rho}{\partial s}\right)_p ds = \frac{1}{a^2}\, dp + \left(\frac{\partial \rho}{\partial s}\right)_p ds. \tag{2.33}$$

The second term is more complex and comes from the friction term that is to be added to the momentum conservation equation. However, the derivation of an exact analytical expression that would allow to incorporate the value of the isentropic efficiencies into the definition of the compound-flow indicator, if possible, is beyond the scope of the present work.

As a first step, it is chosen to assume that although Equation 2.31 does not provide the exact value of β as described by the theory of Bernstein et al. [7] when the flow is non-isentropic, it nevertheless remains an acceptable indicator for the compound-choking phenomenology. Isentropic flows will first be considered, and the assumption will be further discussed in the following chapters when applying the criterion to non-isentropic flows.

Compound waves

The compound-choking phenomenon can also be explained in the frame of compound waves. Hence, it is now proposed to reassert the compound-choking phenomenon from this perspective to physically motivate the application of the theory to ejector, as a possible improvement to the classical choking criterion (i.e. the Fabri-choking criterion). Figure 2.6 shows a magnified view of the flow for one of the streams.

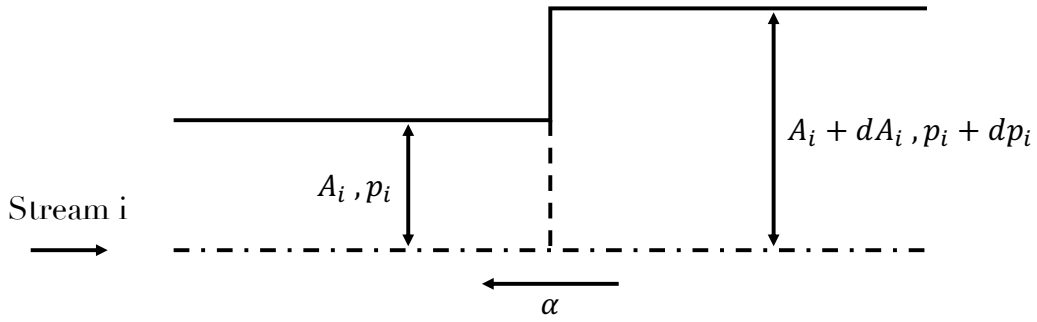

Figure 2.6: Evolution of one stream in a nozzle.

Considering the flow schematic in Figure 2.5, if a small plane pressure disturbance is introduced on the flow, it cannot travel at different speeds inside of the different streams. Otherwise, this would violate the assumption of constant static pressure across each section. The wave must rather be continuous across the streams and travel at a single

speed ; it acts as a compound-wave. The speed of said compound-wave is denoted by α.

Consider now the flow inside of one stream (cfr. Figure 2.6). The flow velocity V_i' in the frame of the compound-wave is :

$$V_i' = V_i + \alpha, \tag{2.34}$$

where V_i is the absolute flow velocity. The compound-wave speed is defined positive when the compound-wave travels upstream. It follows that $\alpha > 0$ corresponds to a compound-subsonic flow ; $\alpha = 0$ corresponds to a compound-sonic flow ; $\alpha < 0$ corresponds to a compound-supersonic flow.

Remaining in the compound-wave frame, the mass and momentum conservation equations read (cfr. Figure 2.6) :

$$\rho_i V_i' A_i = (\rho_i + d\rho_i)(V_i' + dV_i')(A_i + dA_i) = \text{constant}, \tag{2.35}$$

$$p_i A_i - (p_i + dp_i)(A_i + dA_i) + p_i dA_i = \rho_i V_i' A_i \ (V_i' + dV_i' - V_i'). \tag{2.36}$$

Equations 2.35 and 2.36 can then be re-written, respectively, as :

$$\frac{d\rho_i}{\rho_i} + \frac{dV_i'}{V_i'} + \frac{dA_i}{A_i} = 0, \tag{2.37}$$

$$\frac{dp_i}{p_i} + \frac{\rho_i V_i'^2}{p_i}\frac{dV_i'}{V_i'} = 0. \tag{2.38}$$

Also, from the definition of the speed of sound $a_i^2 = \left(\frac{\partial p_i}{\partial \rho_i}\right)_s$, one obtains the following relation, which is valid for isentropic flows :

$$\frac{d\rho_i}{\rho_i} = \frac{1}{a_i^2}\frac{dp_i}{\rho_i}. \tag{2.39}$$

Injecting Equation 2.39 into Equation 2.37 gives, successively :

$$\frac{1}{a_i^2}\frac{dp_i}{\rho_i} + \frac{dV_i'}{V_i'} + \frac{dA_i}{A_i} = 0, \tag{2.40}$$

$$\frac{dV_i'}{V_i'} = -\left(\frac{dA_i}{A_i} + \frac{1}{a_i^2}\frac{dp_i}{\rho_i}\right). \tag{2.41}$$

Then, by injecting Equation 2.41 into Equation 2.38, one gets :

$$\frac{dA_i}{A_i} = \frac{dp_i}{\rho_i}\left(\frac{1}{V_i'^2} - \frac{1}{a_i^2}\right). \tag{2.42}$$

Using the definition of V_i' in Equation 2.34 and the assumption of constant pressure along a given section (i.e. $p_i = p$), one can find :

$$\frac{dA_i}{A_i} = \frac{dp}{\rho_i}\left[\frac{1}{(\alpha + M_i a_i)^2} - \frac{1}{a_i^2}\right]. \tag{2.43}$$

If one further assumes that the variation between two successive cross-sectional areas is small, namely $\sum dA_i \approx 0$, one gets :

$$\sum_{i=1}^{n} \frac{A_i}{\rho_i V_i^2} M_i^2 \approx \sum_{i=1}^{n} \frac{A_i}{\rho_i V_i^2} \frac{1}{\left(\frac{\alpha}{V_i} + 1\right)^2}. \tag{2.44}$$

Introducing the latter relation into Equation 2.31 provides an expression of the compound-flow indicator as a function of the compound-wave speed :

$$\beta = p \sum_{i=1}^{n} \frac{A_i}{\rho_i V_i^2}\left[1 - \frac{1}{\left(\frac{\alpha}{V_i} + 1\right)^2}\right]. \tag{2.45}$$

Note the use of the equal sign in Equation 2.45 instead of the approximate sign. In fact, because β is only an indicator that provides information on the flow regime, the exact value that the compound-flow indicator takes is of little relevance. Only its sign matters. In the case of a compound-sonic flow (i.e. $\beta = 0$) the relation is indeed exactly satisfied because if the flow is isentropic, it is compound-sonic at the throat, where one has $\sum dA_i = 0$. The indicator β thus keeps its full meaning in the frame of the compound-wave. From Equation 2.45 one can define the flow regimes as a function of the compound-wave speed, thus linking α and β :

- $\alpha > 0$: compound-subsonic flow $\rightarrow \beta > 0$.
- $\alpha = 0$: compound-sonic flow $\rightarrow \beta = 0$.
- $\alpha < 0$: compound-supersonic flow $\rightarrow \beta < 0$.

Physically, a compound-wave with $\alpha > 0$ would travel upstream. Likewise, if $\alpha < 0$, it would be pushed downstream by the flow so that no information could reach the upstream flow. This indeed describes well the choking phenomenon of classical nozzle theory. Hence, the choking condition based on the compound-compressible flow theory is given by :

$$\sum_{i=1}^{n} \frac{A_i}{\rho_i V_i^2}\left(1 - M_i^2\right) = 0. \tag{2.46}$$

The compound-choking theory can thus be seen as an extension of the classical choking condition, that would be to impose $M_i = 1$ for all streams. One can plainly see that by doing so, the compound-choking criterion would also be satisfied. This also means that multiple choking solutions can be expected from the compound-choking criterion.

Application to ejectors

Applying the compound-choking criterion to ejectors comes down to considering a two-stream flow, that are, the primary and secondary streams. The theory, from an ejector point of view, indicates that the ejector is choked when one of the streams reaches a particular supersonic velocity, and the other stream reaches a subsonic velocity that ensures Equation 2.31. For supersonic ejectors, the primary flow will be supersonic and the secondary flow subsonic, as the primary flow already reaches supersonic velocities after its expansion in the primary nozzle, thereby constraining the model so that the secondary stream has to be the subsonic one.

One could argue that if the primary flow were to be re-compressed after exiting the primary nozzle, one could in theory have a subsonic primary flow and a supersonic secondary flow solution that would allow $\beta = 0$. This however does not have a physical meaning, as ejectors are entrainment devices, so that the secondary flow velocity should be inferior to that of the primary. In any case, the re-compression of the primary flow would likely happen by means of complex shock structures that are well beyond the modeling capacities of the present thermodynamic model.

In addition, note that as opposed to what was said in the previous subsection, the solution is here unique. In accordance with what is explained just above, the primary flow is supersonic, which suppresses the solution where both flows would be sonic, and since there are only two streams, one can have only one solution. In this section, it is proposed to review the solving algorithm that allows to compute the ejector performance using the compound-choking criterion.

The first step is to guess the value of p_y, as it is impossible to derive the solution in a straightforward manner like when using the Fabri-choking criterion :

$$p_{p,y} = p_{s,y} = p_y = p_{guess}. \tag{2.47}$$

Actually, in order to efficiently find the solution, it was chosen to use a solving scheme similar to the one that was used to find G_{max}. As a reminder, this consists in computing the solution for a limited number of linearly spaced guess pressures, here on p_y. In this case, it is desired to find the solution for $\beta(p_y) = 0$, which is equivalent to finding the minimum of $|\beta(p_y)|$. At each iteration, the left and right limits for the guess vector on p_y is updated and the solution interval narrowed, until a satisfactory precision is reached.

The primary flow properties at section y are found in the same way as for the Fabri-choking, that is, using Equations 2.12 through 2.16. The secondary flow properties are

computed in a similar fashion, but expanding the flow from the secondary stagnation conditions. First, the enthalpy is computed :

$$h_{s,y,is} = h(p_{s,y}, s_{s,0}), \tag{2.48}$$

$$h_{s,y} = h_{s,0} - \eta_s \, (h_{s,0} - h_{s,y,is}). \tag{2.49}$$

The thermodynamic state being defined at section y, the secondary flow density and velocity can be obtained, respectively, as :

$$\rho_{s,y} = \rho(p_{s,y}, h_{s,y}), \tag{2.50}$$

$$V_{s,y} = \sqrt{2(h_{s,0} - h_{s,y})}. \tag{2.51}$$

As can be seen in Equation 2.31, the computation of β also requires the knowledge of the Mach number, and therefore the speed of sound at a given thermodynamic state. As mentioned previously, this can occasionally be an issue when working with two-phase flows because the `COOLPROP` library is flawed. The computation of the speed of sound will be the subject of the following section. For now, let us assume, without loss of generality that :

$$a_{p,y} = a(p_{p,y}, h_{p,y}), \tag{2.52}$$

$$a_{s,y} = a(p_{s,y}, h_{s,y}), \tag{2.53}$$

from which the primary and secondary Mach numbers at section y are computed. Injecting all quantities previously computed into Equation 2.31 gives the expression of the compound-flow indicator for ejectors :

$$\beta = p_y \left(\frac{A_{p,y}}{\left(\rho_{p,y} \, V_{p,y}^2\right)} \left(1 - M_{p,y}^2\right) \; + \; \frac{A_{s,y}}{\left(\rho_{s,y} \, V_{s,y}^2\right)} \left(1 - M_{s,y}^2\right) \right), \tag{2.54}$$

where the secondary flow area at section y was computed using Equation 2.17, which is still applicable to the compound-choking criterion. Once the value of p_y is found with a sufficient precision, all properties at section y are known, and the secondary mass flow rate is computed by :

$$\dot{m}_s = \rho_{s,y} V_{s,y} A_{s,y} \tag{2.55}$$

which allows to determine the on-design entrainment ratio by using Equation 2.19. Figure 2.7 shows the flowchart of the computation algorithm that was described in this section.

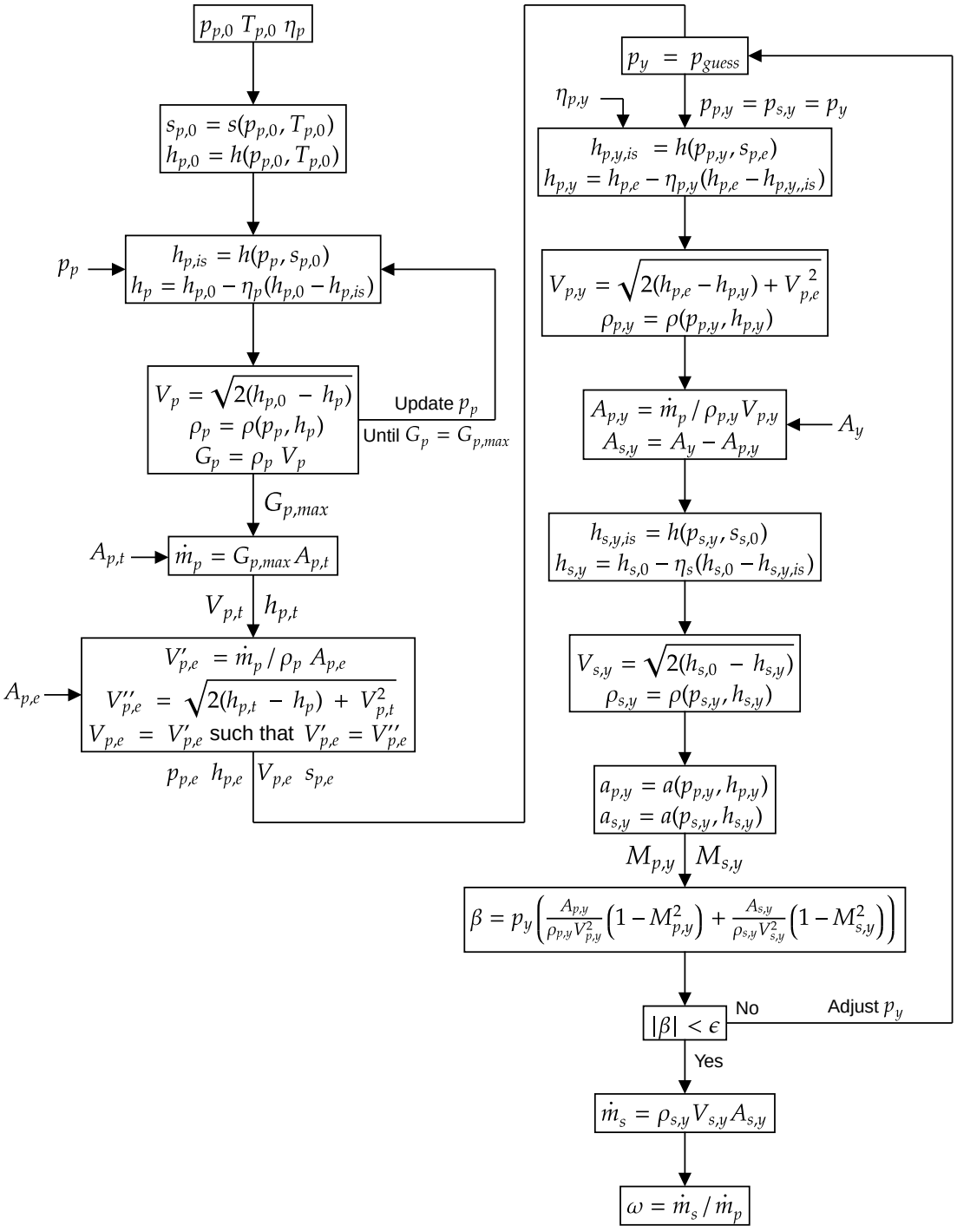

Figure 2.7: Flowchart of the model for on-design operation using the compound-choking criterion (cfr. Figure 2.1). Note that the computation of the critical back pressure will be performed in the following chapter.

2.5 Speed of sound

As mentioned previously, applying the compound-choking criterion requires the computation of the speed of sound, which can be a problem since the COOLPROP library has sometimes issues near the saturation curve. In this section, it is proposed to analyse the problem and provide a solution that could ensure the computation of the speed of sound for any set of thermodynamic properties in an efficient way.

In order to identify more clearly the problematic region, one can try to retrieve the speed of sound using the COOLPROP library for a number of points in a $T-S$ diagram and mark the point where the function generated an error. As an example, such a diagram is shown for R134a in Figure 2.8. The black zones are the regions where COOLPROP failed to provide a value of the speed of sound.

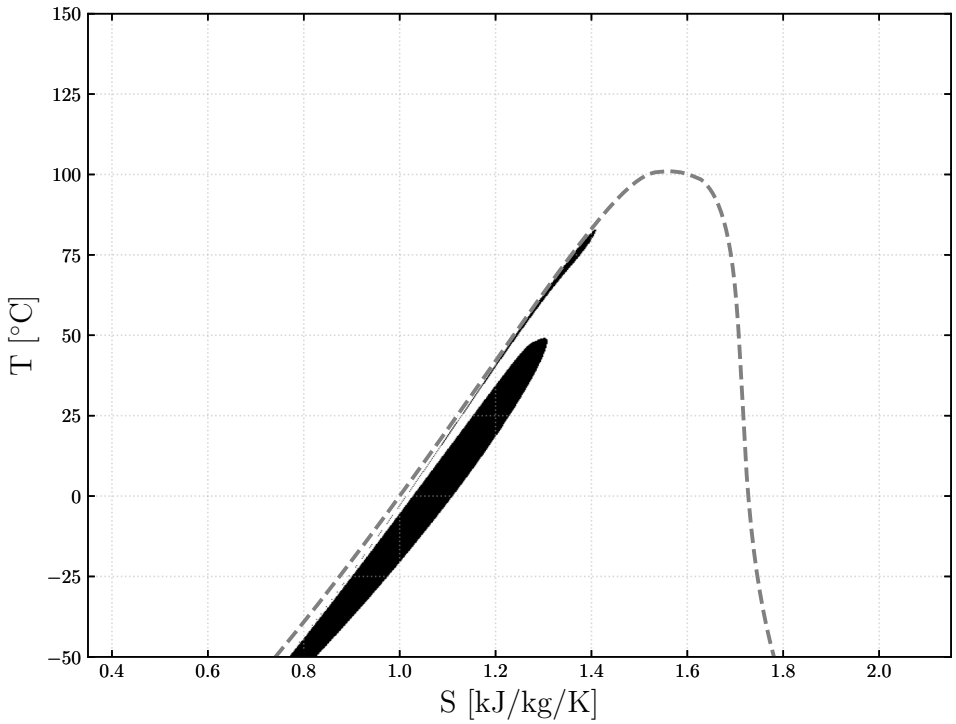

Figure 2.8: $T-S$ diagram for R134a. The black zones are the ones where a could not be computed.

One can see that the problematic region is the saturated liquid-vapour region, and more specifically the area underneath the saturated liquid curve. In addition, note that COOLPROP also has issues near the critical point that can prevent the computation of any thermodynamic quantity. This is due to the implementation and computation algorithm used by the COOLPROP library. For example, retrieving the entropy from the pressure and

enthalpy near the critical point might work, whereas requesting the entropy given the temperature and density might lead to an error.

Moreover, it was observed that COOLPROP is sometimes able to return a value of the speed of sound, but the latter is completely false, taking extremely high values. This happens near the border of the problematic region depicted in Figure 2.8. For this reason, it was chosen to propose an alternative to the speed of sound values given by the tabulated data.

Two options were considered to circumvent the faulty computation of the speed of sound underneath the saturation curve. The first approach consists in using finite differences to evaluate the speed of sound. The second one is to implement a method based on the maximisation of the mass flux. This latter method however, worked well in the non-problematic regions but had issues at the same locations where COOLPROP cannot provide a solution for the speed of sound. This is due to the fact that the gradients of thermodynamic properties near the saturated liquid curve are very steep. To this adds the fact that the library itself is not very robust in that region.

It is now proposed to review the finite difference method that was implemented. First, coming back to the definition of the speed of sound :

$$a = \sqrt{\left(\frac{\partial p}{\partial \rho}\right)_s}, \tag{2.56}$$

one can compute an approximate value for the speed of sound using centered finite differences with :

$$a(p,s) = \sqrt{\left(\frac{\Delta p}{\Delta \rho}\right)_s}, \tag{2.57}$$

where Δp has to be chosen sufficiently small so that the precision of the derivative is satisfactory, and sufficiently large so that there is no loss in precision on $\Delta\rho$ due the finite machine precision. $\Delta\rho$ is computed by :

$$\Delta\rho = \rho\left(p + \frac{\Delta p}{2}, s\right) - \rho\left(p - \frac{\Delta p}{2}, s\right). \tag{2.58}$$

Of course, this alternate computation method is unnecessary in the region where the COOLPROP library has no issues. This method will therefore only be used when computing the speed of sound of a saturated liquid-vapour mixture. In other words, the computation of the speed of sound relies on an hybrid method that uses the data directly retrieved from COOLPROP if the thermodynamic state for which a is needed is outside of the saturated liquid-vapour region, and the finite difference method otherwise. In addition, the finite difference method is also used as a back-up, if COOLPROP fails to

provide a solution. The choice of an hybrid method is motivated by the fact that retrieving a quantity from COOLPROP is faster than using finite differences.

Figure 2.9 shows the speed of sound for R134a in a $T-S$ diagram using the hybrid method that is presently described. First, one can observe that, as desired, the speed of sound can be computed for any thermodynamic state. Furthermore, there appears to be a very steep gradient at the location of the saturated liquid curve. This is likely due to the fact that the isobars are very close to each other near the saturated liquid curve.

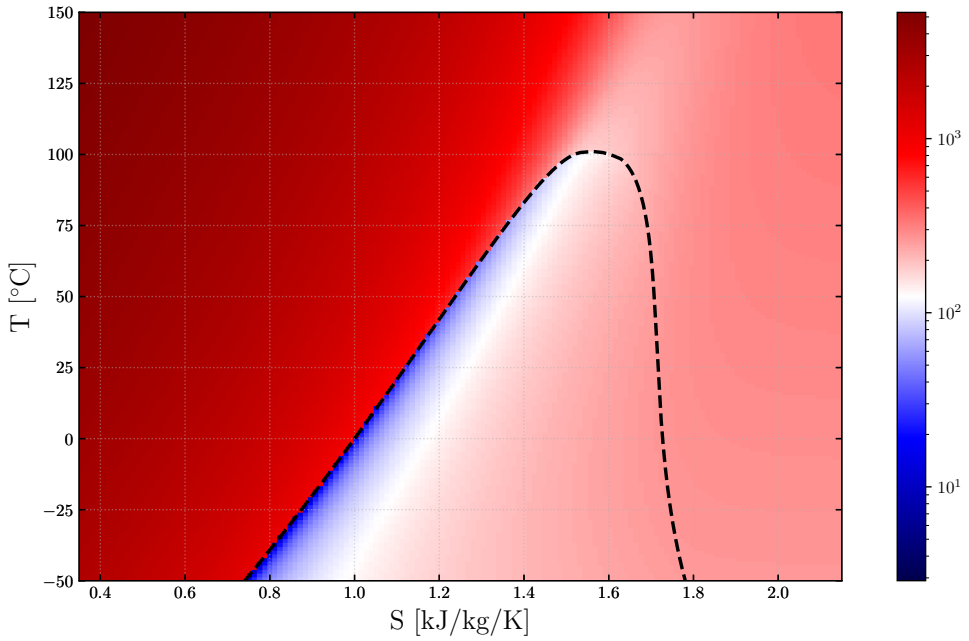

Figure 2.9: Speed of sound a [m/s] on a $T-S$ diagram for R134a using the hybrid method. Note that the color map is in logarithmic scale.

The finite difference method was found to provide a relative error of maximum 1e-7 % compared to the tabulated data provided by COOLRPOP. Of course, it is impossible to evaluate the error at the location of the problematic region, but the fact that the gradient appears to be smooth is a good indicator that the method provides good results.

Note at this point that this hybrid method was implemented in order to avoid potential problems if the present work should be applied to two-phase flows where flashing occurs. The hybrid method was developed to provide clean results, unhindered by the potential flaws of COOLPROP. However, in what follows, the working fluids are superheated gases, for which the COOLPROP library provides excellent results. Therefore the finite difference

method has not been used for the results presented in this document.

2.6 Results

It is now proposed to review the accuracy of the on-design model for both choking criteria. The difference between the perfect gas model of Lamberts et al. [25] and the present model – that uses real gas properties along with the compound-choking criterion – will also be quantified. Note that all thermodynamic transformations in this section are assumed to be isentropic.

The predictions of the model for the entrainment ratio will be compared to the experimental results of Huang et al. [20] using R141b as working fluid. Those results are convenient to assess the performance of the method, as they offer data for various geometries and various operating conditions. Two different primary nozzles are combined with eight mixing chambers, and eleven different geometries are used for the experiments. The nozzle and mixing chamber combinations are codified using two letters. The first one corresponds to the primary nozzle geometry (A or E) and the second one to the mixing chamber geometry (A through H). The associated dimensions can be found in the original article, should the reader be interested. The two nozzles differ from their throat and exit areas [20], and the mixing chambers from the area of the constant area section and the inlet converging angle. The area ratios A_y/A_t that are used vary from 6.44 to 10.64. The primary stagnation pressure varies from 4 to 6.04 [bar] and the secondary stagnation pressure from 0.4 to 0.47 [bar]. In addition, the fluids at both inlets are in a state of saturated vapour. As pointed out in the original article [20], R141b has a positive-slope saturated-vapor line in the thermodynamic T–S diagram. Hence, when the vapour expands in the ejector, it does not condense and the flow remains single phase.

2.6.1 Fabri-choking

Results provided by the model, using the *Fabri-choking* criterion, are compared to the experimental data in Table 2.1. The relative error is defined as :

$$\text{Error} = \frac{\omega_{mod} - \omega_{exp}}{\omega_{exp}}, \tag{2.59}$$

with ω_{exp} and ω_{mod} the entrainment ratios obtained from the experiment and the model, respectively. As can be seen, the model provides very poor results, with relative errors that can reach values up to 53.09% for case 10 and a mean error of 17.54%. It also appears very clearly that the model tends to underestimate the entrainment ratio. The general trend observed is that the error becomes greater as the area ratio A_y/A_t becomes smaller. In

Case	Ejector	A_y/A_t	$p_{p,0}$ [bar] ($T_{sat}[^\circ C]$)	$p_{s,0}$ [bar] ($T_{sat}[^\circ C]$)	ω (exp)	ω (model)	Error [%]
1	EH	10.64	6.04 (95)	0.4 (8)	0.4377	0.3957	-9.60
2	EF	9.83	6.04 (95)	0.4 (8)	0.3937	0.3362	-14.61
3	AD	9.41	6.04 (95)	0.4 (8)	0.3457	0.3054	-11.66
4	EE	9.17	6.04 (95)	0.4 (8)	0.3505	0.2877	-17.92
5	AC	8.28	6.04 (95)	0.4 (8)	0.2814	0.2223	-21.00
6	ED	8.25	6.04 (95)	0.4 (8)	0.2902	0.2201	-24.16
7	EC	7.26	6.04 (95)	0.4 (8)	0.2273	0.1474	-35.15
8	AG	7.73	6.04 (95)	0.4 (8)	0.2552	0.1819	-28.72
9	EG	6.77	6.04 (95)	0.4 (8)	0.2043	0.1114	-45.47
10	AA	6.44	6.04 (95)	0.4 (8)	0.1859	0.0872	-53.09
11	AD	9.41	5.38 (90)	0.4 (8)	0.4446	0.3797	-14.60
12	AC	8.28	5.38 (90)	0.4 (8)	0.3488	0.2879	-17.46
13	AG	7.73	5.38 (90)	0.4 (8)	0.304	0.2417	-20.49
14	AB	6.99	5.38 (90)	0.4 (8)	0.2718	0.1809	-33.44
15	AA	6.44	5.38 (90)	0.4 (8)	0.2246	0.1357	-39.58
16	AD	9.41	4.65 (84)	0.4 (8)	0.5387	0.4865	-9.69
17	AC	8.28	4.65 (84)	0.4 (8)	0.4241	0.3797	-10.47
18	AG	7.73	4.65 (84)	0.4 (8)	0.3883	0.3276	-15.63
19	AB	6.99	4.65 (84)	0.4 (8)	0.3117	0.2577	-17.32
20	AA	6.44	4.65 (84)	0.4 (8)	0.288	0.2057	-28.58
21	AD	9.41	4.00 (78)	0.4 (8)	0.6227	0.6142	-1.37
22	AC	8.28	4.00 (78)	0.4 (8)	0.4889	0.4907	0.37
23	AG	7.73	4.00 (78)	0.4 (8)	0.4393	0.4306	-1.98
24	AB	6.99	4.00 (78)	0.4 (8)	0.3922	0.3497	-10.84
25	AA	6.44	4.00 (78)	0.4 (8)	0.3257	0.2895	-11.11
26	EF	9.83	6.04 (95)	0.47 (12)	0.4989	0.4456	-10.68
27	EE	9.17	6.04 (95)	0.47 (12)	0.4048	0.3889	-3.93
28	AD	9.41	6.04 (95)	0.47 (12)	0.4541	0.4095	-9.82
29	AG	7.73	6.04 (95)	0.47 (12)	0.3503	0.2654	-24.24
30	EC	7.26	6.04 (95)	0.47 (12)	0.304	0.2251	-25.95
31	AA	6.44	6.04 (95)	0.47 (12)	0.235	0.1547	-34.17
32	AD	9.41	5.38 (90)	0.47 (12)	0.5422	0.497	-8.34
33	AG	7.73	5.38 (90)	0.47 (12)	0.4034	0.3359	-16.73
34	AA	6.44	5.38 (90)	0.47 (12)	0.2946	0.2121	-28.00
35	AD	9.41	4.65 (84)	0.47 (12)	0.635	0.6226	-1.95
36	AG	7.73	4.65 (84)	0.47 (12)	0.479	0.4371	-8.75
37	AA	6.44	4.65 (84)	0.47 (12)	0.3398	0.2946	-13.30
38	AD	9.41	4.00 (78)	0.47 (12)	0.7412	0.7727	4.25
39	AG	7.73	4.00 (78)	0.47 (12)	0.6132	0.5582	-8.97

Table 2.1: Predictions of the entrainment ratio for the ejector configurations of Huang et al. [20] using the Fabri-choking criterion.

addition, note that no correlation between the inlet converging angle and the accuracy of the model was found.

Figure 2.10 shows the entrainment ratio predicted by the model versus the experimental data. It can be seen that the worst results are found for low values of the entrainment ratio. Those cases also correspond to the smallest area ratios A_y/A_t, in accordance with the previous observation. For values of ω superior to 0.3, most predictions have a deviation of maximum 20% and seem to reach the experimental values in an asymptotic way. For lower values, the model largely diverges.

The poor results provided by the model using the Fabri-choking criterion are likely explained by the restrictive assumption that the mixing pressure p_y is constant along section y. Indeed, the fact that the secondary pressure has to match the primary pressure may hinder the secondary mass flow rate. This will be further discussed in the following subsection.

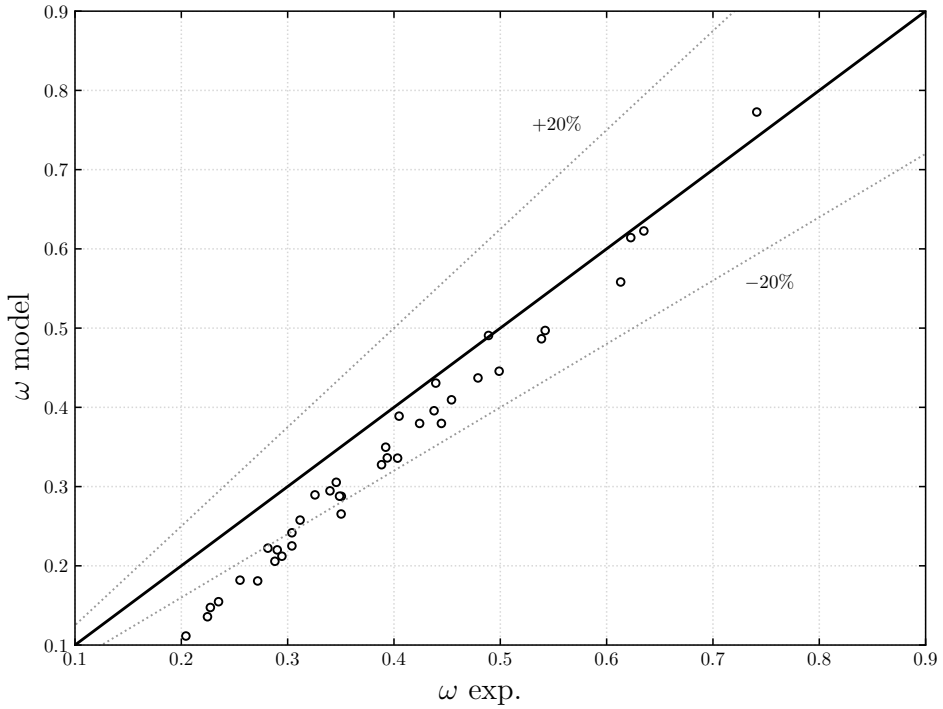

Figure 2.10: Comparison of the Fabri-choking with the experiment of Huang et al. [20].

2.6.2 Compound-choking

Comparison between perfect and real gas models

Before comparing the model to the experiment, the real gas model can be compared to the perfect gas model introduced by Lamberts et al. [25] in order to quantify the difference and potential gain in accuracy. As a reminder, the model of Lamberts et al. [25] is an analytical on-design model that uses the compound-choking criterion. Figure 2.11 shows the relative difference between the perfect gas model of Lamberts et al. and the present – real gas – model, for various stagnation pressure ratios and as a funtion of the area ratio A_y/A_t. Air is chosen as working fluid for this comparison, as it can reasonably be considered as a perfect gas. For the model of Lamberts et al. [25], the heat capacity ratio and the specific gas constant are chosen as, respectively, $\gamma = 1.4$ and $R = 287.1$ [J/kg/K].

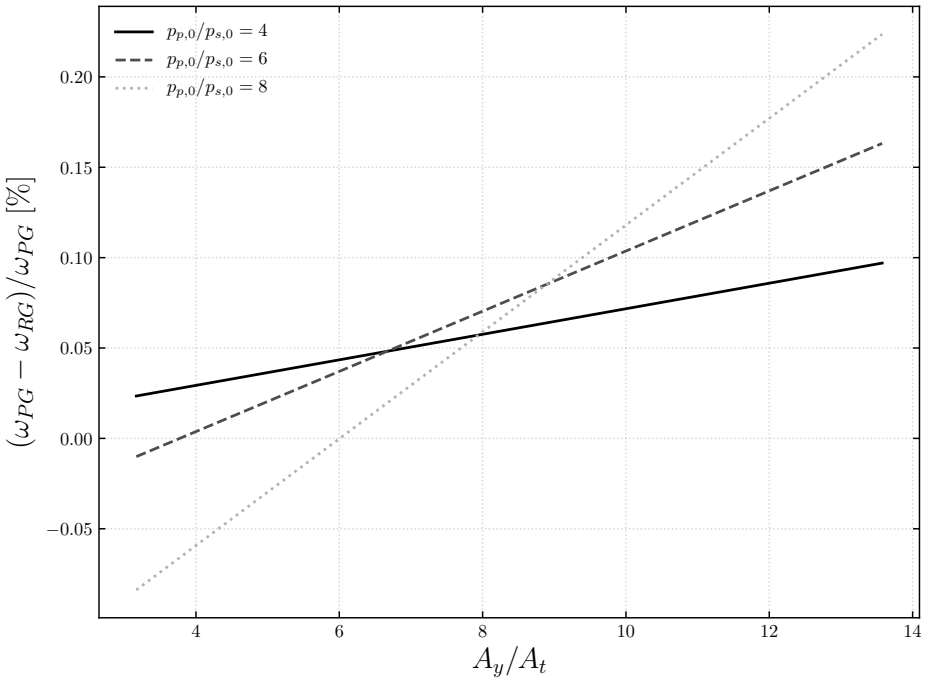

Figure 2.11: Relative difference between the entrainment ratios predicted by the perfect gas model ω_{PG} of Lamberts et al. [25] and the real gas model ω_{RG}, using the compound-choking criterion. The working fluid is air and $p_{s,0} = 1$ [bar].

As can be seen on the above Figure, the relative difference is quite small, with a maximum of approximately 0.2% over the range of area ratios presented here. This range of A_y/A_t is quite representative and includes most of the geometries that can be found in the

literature. The limited difference between the present model and the perfect gas analytical model firstly indicates that the present model has been correctly implemented. Then, one can observe that the difference linearly increases as the area ratio gets higher, and that said difference grows faster the greater the stagnation pressure ratio gets. This may be explained by the fact that the perfect gas model uses a constant heat capacity ratio γ of 1.4 in the present case of air. To this adds the error caused by the introduction of the perfect gas equation of state into the model of Lamberts et al. [25]. Indeed, as the primary pressure gets higher (i.e. the molecular interactions get stronger), the perfect gas equation of state looses in accuracy because air is not actually a perfect gas. The difference between the two models can mainly be traced back to a difference in the mixing pressure p_y, that is directly used to compute the secondary mass flow rate and therefore the entrainment ratio.

Comparison with experimental results

Once again, the predictions of the model are compared to the experimental data of Huang et al. [20] in Table 2.2. The results provided by the compound-choking theory are much better than those predicted by the Fabri-choking theory. However, much as was observed for the Fabri-choking, predictions are better for higher values of A_y/A_t. The compound-choking criterion also tends to underestimate the entrainment ratio, but to a lesser extent. This slight underestimation is positive from a design perspective, as it is conservative.

Figure 2.12 shows the entrainment ratio predicted by the model versus the experimental results. One may observe that the better part of the predictions lie within a 10% error from the experimental data, with a mean error of 5.28%. Again, the model appears to become less accurate as the entrainment ratio gets lower, although it does not seem to clearly diverge in this region, as could be observed in Figure 2.9 for the Fabri-choking.

In addition, one can also see from Table 2.2 that for fixed stagnation conditions, results seem to be better when the stagnation pressure ratio $p_{p,0}/p_{s,0}$ gets smaller. This is consistent with the observations of Lamberts [23]. Indeed, as the author pointed out, the main limiting factor of the theory is that the pressure can only vary along the nozzle and is equal for the primary and secondary flows at each section. This is not necessarily the case for real ejectors, and Lamberts [23] found a correlation between the error and the stagnation pressure ratio.

Moreover, for a given geometry, a lower stagnation pressure ratio may also lead to having primary and secondary mixing pressures that are closer to each other (in real ejectors), therefore limiting the error caused by the constant pressure assumption. Although a

Case	Ejector	A_y/A_t	$p_{p,0}$ [bar] ($T_{sat}[^\circ C]$)	$p_{s,0}$ [bar] ($T_{sat}[^\circ C]$)	ω (exp)	ω (model)	Error [%]
1	EH	10.64	6.04 (95)	0.4 (8)	0.4377	0.4302	-1.71
2	EF	9.83	6.04 (95)	0.4 (8)	0.3937	0.3737	-5.08
3	AD	9.41	6.04 (95)	0.4 (8)	0.3457	0.3446	-0.32
4	EE	9.17	6.04 (95)	0.4 (8)	0.3505	0.3281	-6.39
5	AC	8.28	6.04 (95)	0.4 (8)	0.2814	0.2674	-4.98
6	ED	8.25	6.04 (95)	0.4 (8)	0.2902	0.2654	-8.55
7	EC	7.26	6.04 (95)	0.4 (8)	0.2273	0.1994	-12.27
8	AG	7.73	6.04 (95)	0.4 (8)	0.2552	0.2305	-9.68
9	EG	6.77	6.04 (95)	0.4 (8)	0.2043	0.1676	-17.96
10	AA	6.44	6.04 (95)	0.4 (8)	0.1859	0.1466	-21.14
11	AD	9.41	5.38 (90)	0.4 (8)	0.4446	0.4156	-6.52
12	AC	8.28	5.38 (90)	0.4 (8)	0.3488	0.328	-5.96
13	AG	7.73	5.38 (90)	0.4 (8)	0.304	0.286	-5.92
14	AB	6.99	5.38 (90)	0.4 (8)	0.2718	0.2304	-15.23
15	AA	6.44	5.38 (90)	0.4 (8)	0.2246	0.1898	-15.49
16	AD	9.41	4.65 (84)	0.4 (8)	0.5387	0.5186	-3.73
17	AC	8.28	4.65 (84)	0.4 (8)	0.4241	0.4164	-1.82
18	AG	7.73	4.65 (84)	0.4 (8)	0.3883	0.3672	-5.43
19	AB	6.99	4.65 (84)	0.4 (8)	0.3117	0.3018	-3.18
20	AA	6.44	4.65 (84)	0.4 (8)	0.288	0.254	-11.81
21	AD	9.41	4.00 (78)	0.4 (8)	0.6227	0.6428	3.23
22	AC	8.28	4.00 (78)	0.4 (8)	0.4889	0.5234	7.06
23	AG	7.73	4.00 (78)	0.4 (8)	0.4393	0.4658	6.03
24	AB	6.99	4.00 (78)	0.4 (8)	0.3922	0.3889	-0.84
25	AA	6.44	4.00 (78)	0.4 (8)	0.3257	0.3325	2.09
26	EF	9.83	6.04 (95)	0.47 (12)	0.4989	0.479	-3.99
27	EE	9.17	6.04 (95)	0.47 (12)	0.4048	0.4249	4.97
28	AD	9.41	6.04 (95)	0.47 (12)	0.4541	0.4445	-2.11
29	AG	7.73	6.04 (95)	0.47 (12)	0.3503	0.3085	-11.93
30	EC	7.26	6.04 (95)	0.47 (12)	0.304	0.2712	-10.79
31	AA	6.44	6.04 (95)	0.47 (12)	0.235	0.2073	-11.79
32	AD	9.41	5.38 (90)	0.47 (12)	0.5422	0.529	-2.43
33	AG	7.73	5.38 (90)	0.47 (12)	0.4034	0.3752	-6.99
34	AA	6.44	5.38 (90)	0.47 (12)	0.2946	0.2601	-11.71
35	AD	9.41	4.65 (84)	0.47 (12)	0.635	0.6512	2.55
36	AG	7.73	4.65 (84)	0.47 (12)	0.479	0.4723	-1.40
37	AA	6.44	4.65 (84)	0.47 (12)	0.3398	0.3375	-0.68
38	AD	9.41	4.00 (78)	0.47 (12)	0.7412	0.7981	7.68
39	AG	7.73	4.00 (78)	0.47 (12)	0.6132	0.5895	-3.86

Table 2.2: Predictions of the entrainment ratio for the ejector configurations of Huang et al. [20] using the compound-choking criterion.

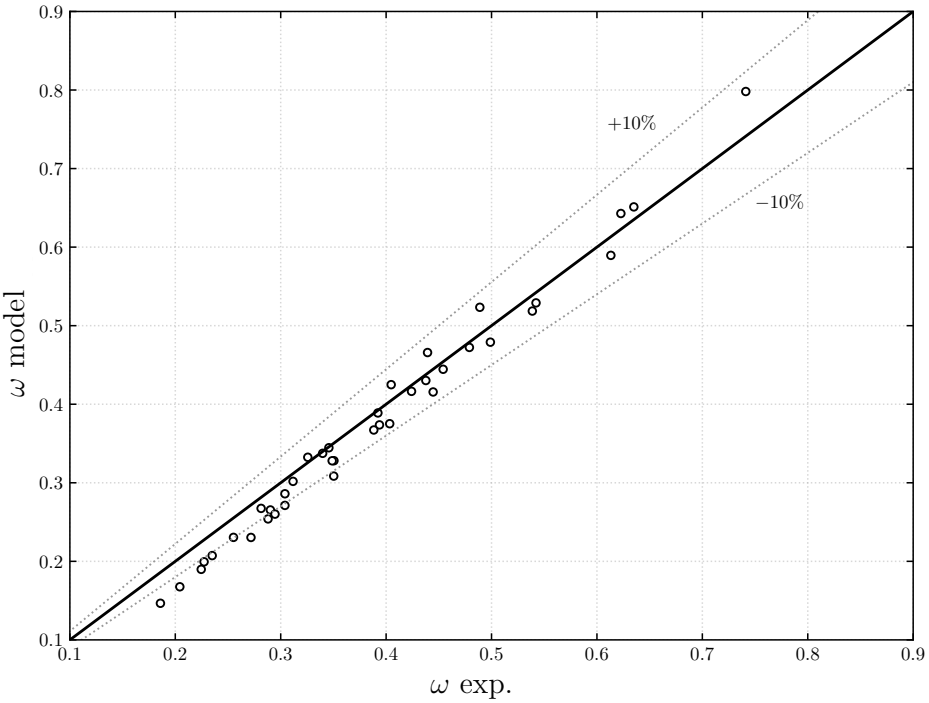

Figure 2.12: Comparison of the compound-choking with the experiment of Huang et al. [20].

thorough investigation has not been performed, it was found that for case 25 of the experiments of Huang et al. [20] ($p_{p,0}$ = 4 [bar], $p_{s,0}$ = 0.4 [bar]), the primary nozzle exit pressure $p_{p,e}$ was found to be quite close to that of the secondary stagnation pressure : $p_{p,e}$ = 0.33 [bar]. It can, as a first approximation, be assumed that the secondary flow pressure at section e is equal to the secondary stagnation pressure. In reality, it would be slightly lower. On the other hand, for case 10, ($p_{p,0}$ = 6.04 [bar], $p_{s,0}$ = 0.4 [bar]) one has $p_{p,e}$ = 0.51 [bar]. Since the prediction for case 25 is much better than for case 10, this may explain why the model produces better predictions as the stagnation pressure ratio gets lower.

The better performance obtained using the compound-choking criterion comes from a better prediction of the mixing pressure p_y, as this parameter itself defines, for fixed stagnation conditions and geometry, the entrainment ratio in the case of isentropic flows. Nevertheless, it was also observed that the predictions of the present model were not actually better than the ones of the perfect gas model of Lamberts et al. [25]. It was rather found that the perfect gas model overestimated the entrainment ratio, whereas the real gas model underestimated it. This can be visualised in Figure 2.13 where cases 1 through 10 of the experiments of Huang are plotted along with both perfect and real gas model predictions. The fact that the real gas model consistently provides lower entrainment

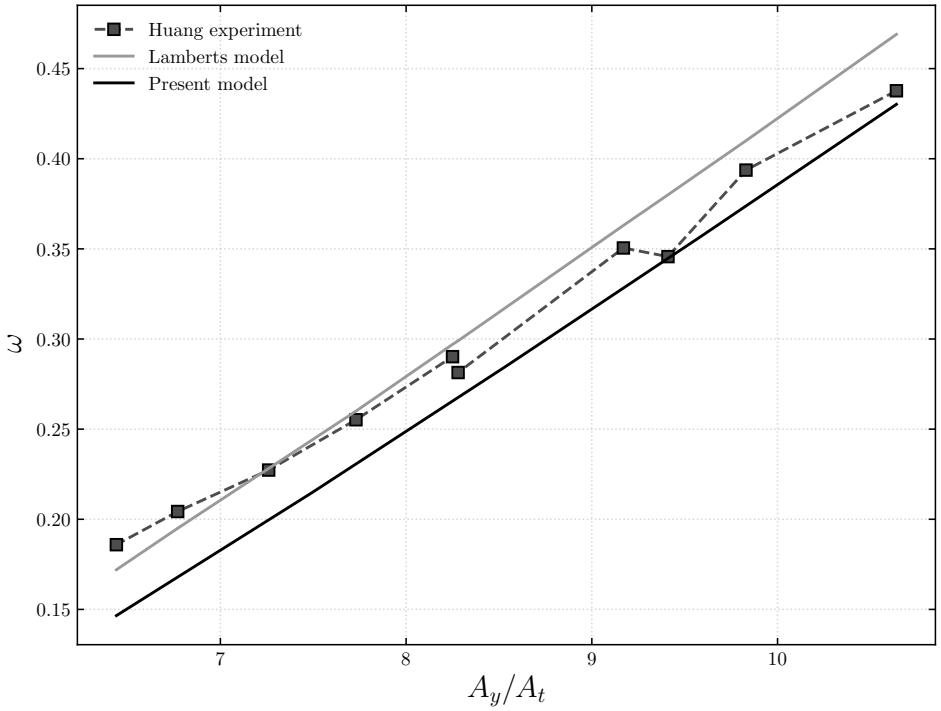

Figure 2.13: Comparison of the entrainment ratio returned by the perfect gas and real gas models with the experiments of Huang et al. [20] at $p_{p,0} = 6.04$ [bar], $p_{s,0} = 0.4$ [bar].

ratios compared to the perfect gas model could be expected, as real gas properties should have limiting effects.

The entrainment ratio essentially appears as a linear function of the area ratio A_y/A_t, and the present model seems to get closer to the experimental results as this ratio gets higher (cfr. Figure 2.13). On the other hand, the perfect gas model seems to better fit the data for low area ratios. Nevertheless, the performance of both models still seem to largely depend on operating conditions. Indeed, it can be seen in Figure 2.14, for cases 21 through 25 of Huang et al. [20], that in this particular scenario, the real gas model performs quite well, even overestimating the entrainment ratio, whereas the perfect gas model provides poorer results.

Lastly, it can be observed, throughout the results of this section (cfr. Tables 2.1 and 2.2), that predictions from the compound-choking theory are consistently higher than that of the Fabri-choking. This will be further discussed in the following chapter.

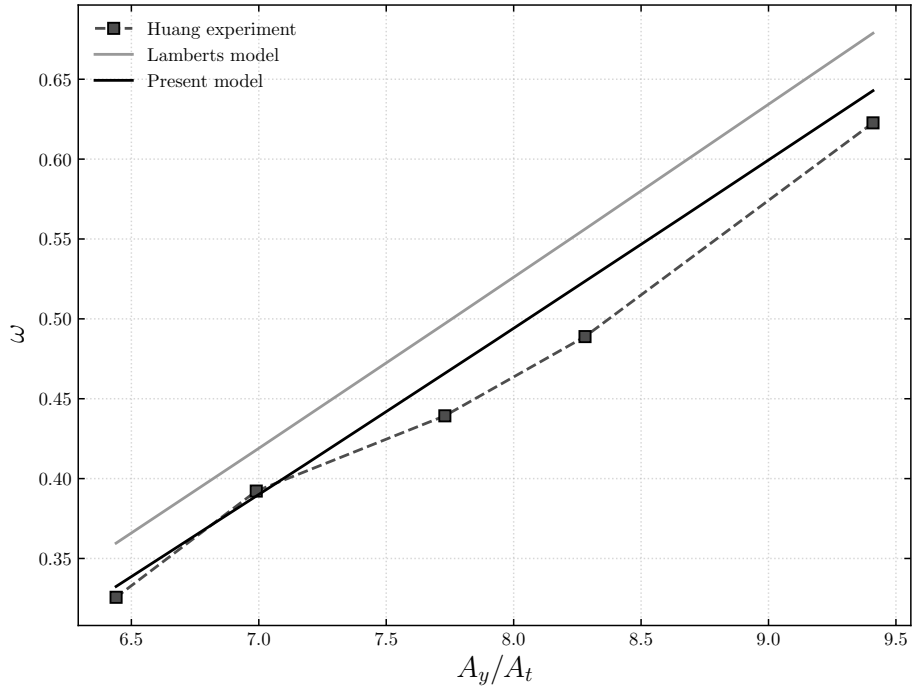

Figure 2.14: Comparison of the entrainment ratio returned by the perfect gas and real gas models with the experiments of Huang et al. [20] at $p_{p,0} = 4.0$ [bar], $p_{s,0} = 0.4$ [bar].

2.7 Conclusion

In this chapter, two on-design models were described. The first model used the Fabri-choking criterion to assess the performance of the ejector. It was found that although this criterion is the most widely used in the literature, it provides quite poor results with the assumption of isentropic flow. The real gas model of Chen et al. [12], which is very similar to the one that was implemented in this work, predicts results that are closer to the experiment but with the use of quite severe isentropic efficiencies (i.e. $\eta_p = 0.92$, $\eta_{p,y} = 0.8$, $\eta_s = 0.85$).

The second model used the compound-choking criterion. It was first validated against the original perfect gas model of Lamberts et al. [25] for air, and very little difference was found between the two models. It was found that the model provided significantly better results than that of the Fabri-choking criterion. This may lead to believe that the compound-choking theory better describes the ejector choking phenomenon. It was then observed that the present model tends to underestimate the entrainment ratio and consistently provides predictions that are lower than the perfect gas model of Lamberts et al. [25].

An alternative method of computation of the speed of sound was also proposed, in order to circumvent the flaws of the COOLPROP library near the saturated liquid curve. It was found that an hybrid method using both the direct tabulated data of COOLPROP and the proposed method allowed to efficiently compute the speed of sound for any thermodynamic state.

CHAPTER 3

Off-design thermodynamic model

3.1 Introduction

In this chapter, it is proposed to review the off-design thermodynamic model that has been implemented. First, the off-design part of the model of Chen et al. [12] will be implemented and a comparison between Fabri-choking and compound-choking for all ejector operating modes will be performed. This will shed light onto a modelling issue inherent to the model of Chen et al. [12], and a corrected version of the model will subsequently be described. A detailed investigation of the connection between the characteristic curves obtained for both choking criteria will then be performed. This will allow to obtain a better physical understanding of the two choking criteria and comfort the idea that the compound-choking criterion might be more adequate to model the flow within a supersonic ejector.

3.2 Off-design operation

The basis of the model that has been implemented is, as for the on-design operation that was reviewed in the previous chapter, the model of Chen et al. [12], for which the main assumptions have already been listed. Unlike in on-design operation, the ejector performance depends on downstream conditions (i.e. the back pressure p_{out}). Indeed, if the ejector is operating in off-design regime, information will travel from the end of the diffuser up to the mixing section. This will have the effect of rising the mixing pressure p_y compared to when the ejector works in on-design operation, therefore modifying the secondary mass flow rate. The entrainment ratio will thus be dependant on the back pressure.

3.2.1 Constant area duct and diffuser

Critical back pressure

As mentioned in the previous chapter, for on-design operation, it is not required to solve the flow downstream of section y in order to compute the entrainment ratio. This is not true if one wishes to obtain ω for a particular back pressure. In order to determine the ejector regime and, if necessary, compute the entrainment ratio for off-design operation, the flow has to be solved up the the diffuser exit, i.e. section d (cfr. Figure 2.1). As a reminder, the condition for the ejector to be in on-design regime is given by :

$$p_{out} < p^*_{out} \ , \tag{3.1}$$

where p^*_{out} is the critical back pressure. Hence, the critical back pressure has to be computed to assess the operating regime. First, the thermodynamic states and velocities of the primary and secondary flows are computed using the on-design model, that is, using either the Fabri-choking or the compound-choking theory. Then, properties are computed at section m, that is the particular section, located inside of the constant area duct, at which primary and secondary flows are assumed to be completely mixed. State m therefore constitutes one single state, without any distinction between the two flows. First, the assumption of constant mixing pressure is used :

$$p_m = p_y. \tag{3.2}$$

Then, the flow speed is computed from the conservation of momentum :

$$V_m = \eta_m \ \frac{\dot{m}_p V_{p,y} + \dot{m}_s V_{s,y}}{\dot{m}_p + \dot{m}_s}. \tag{3.3}$$

where η_m is a mixing efficiency that takes into account the friction losses in the constant area duct due to the combined effect of friction between primary and secondary flows, and friction against the ejector wall. If the ejector is choked, it is assumed that $\eta_m = \psi_m$ with ψ_m a *constant* friction coefficient. The enthalpy can then be found from the conservation of total enthalpy :

$$h_m = \frac{\dot{m}_p h_{p,0} + \dot{m}_s h_{s,0}}{\dot{m}_p + \dot{m}_s} - \frac{V_m^2}{2}. \tag{3.4}$$

State m is now fully defined. After mixing, the flow may or may not be supersonic. However, it has to be subsonic when entering the diffuser, otherwise the diffuser would actually act as a divergent nozzle, thereby accelerating the flow. However, the goal is recover the pressure at the ejector exit. For the 0-D model, it was chosen to re-compress the flow through a single normal shock located at the end of the constant area duct (i.e. at section N). As discussed previously, in real applications, the flow goes through more complex

phenomena, that cannot be taken into account by the present model.

Because the flow may already be subsonic upon section m, it was chosen to check the Mach number at said section and compute the normal shock only if $M_m > 1$. Indeed, if the flow at section m is subsonic, it is unnecessary to solve the equations of a normal shock. In that case, the subsonic flow at the diffuser inlet (i.e. section 2, cfr. Figure 2.1) is indistinguishable from the flow at section m. On the other hand, if the flow is indeed supersonic at section m, the mass, momentum and total enthalpy conservation equations have to be solved to compute the flow at section 2. This has to be performed using an iterative scheme. First, the fluid density is guessed at section 2 :

$$\rho_2 = \rho_{guess} \ , \tag{3.5}$$

with ρ_{guess} chosen higher than ρ_m. The flow speed is then computed from the conservation of mass :

$$V_2 = \frac{\rho_m \, V_m}{\rho_2}. \tag{3.6}$$

From conservation of total enthalpy, the enthalpy is computed :

$$h_2 = h_m + \frac{V_m^2}{2} - \frac{V_2^2}{2}, \tag{3.7}$$

and the pressure at section 2 is obtained from tabulated data by :

$$p_2 = p(\rho_2, h_2). \tag{3.8}$$

The momentum conservation equation is then used to update the value of ρ_2 that was initially guessed :

$$\rho_2 = \frac{\left(\rho_m V_m^2 + p_m - p_2\right)}{V_2^2}. \tag{3.9}$$

The latter value of ρ_2 is then re-injected in Equation 3.6 and re-computed until convergence. State 2 being fully defined, the last step is to solve the flow within the diffuser. To this end, one must first retrieve the entropy at section 2 from tabulated data :

$$s_2 = s(p_2, h_2). \tag{3.10}$$

The enthalpy at the diffuser exit (i.e. section d) for an isentropic compression is found by combining the total enthalpy conservation equation with the classical definition of the isentropic efficiency η_d :

$$h_d = h_2 + \frac{V_2^2}{2} \qquad , \qquad \eta_d = \frac{h_{d,is} - h_2}{h_d - h_2}, \tag{3.11}$$

$$h_{d,is} = h_2 + \eta_d \frac{V_2^2}{2}, \tag{3.12}$$

where the assumption of negligible flow velocity at section d was used. The pressure at the diffuser exit can finally be computed by :

$$p_d = p(h_{d,is}, s_2), \tag{3.13}$$

as the end pressure for the isentropic expansion is the same as that of the non-isentropic one. Since the flow is choked, the computed pressure p_d actually corresponds to the critical back pressure p^*_{out}.

Off-design back pressure

For a given back pressure p_c, one can now determine if the ejector is working in on or off-design regime. For the latter case, the pressure at the end of the diffuser must match the back pressure, which requires one to solve the flow in an iterative way until finding the pressure p_y that satisfies :

$$\frac{p_{out} - p_c}{p_c} < \epsilon, \tag{3.14}$$

with ϵ the error tolerance. As mentioned previously, the mixing pressure p_y gets higher as the back pressure gets higher when the ejector is working in off-design regime. The pressure p_y is therefore updated at each iteration by :

$$p_{y,i+1} = p_{y,i} + k(p_c - p_d) \tag{3.15}$$

with k a proportionality constant that was found to make the iterative loop converge for $k = 0.1$. For the first iteration, the pressures p_y and p_d are equal to the values at the critical point, i.e. p^*_y and p^*_{out}, respectively.

Then, the secondary flow properties at section y are computed using Equations 2.48 through 2.51. Likewise, the primary flow properties are computed from Equations 2.12 through 2.16, and the secondary flow area is computed using Equation 2.17. The secondary mass flow rate associated to that particular value of p_y is then computed from Equation 2.55 and the entrainment ratio from Equation 2.19. In fact, the entrainment ratio is computed in the exact same way as for the on-design operation. For a given ejector, the mixing pressure suffices to determine ω.

The flow conditions at section m are then computed. This is done in the same way as described in the previous section for on-design operating conditions, using Equations 3.2

through 3.4. However, the mixing efficiency η_m is this time a linear function of the back pressure :

$$\eta_m = \psi_m \left(1 - \frac{p_c - p^*_{out}}{p_c}\right) \tag{3.16}$$

This latter expression was proposed by Chen et al. [12]. Note that having a mixing efficiency that is linearly decreasing with the back pressure is the foundation of their off-design model, as it allows for the entrainment ratio to decrease as p_{out} increases. The off-design model of Chen et al. [12] would not work without this dynamic mixing efficiency.

The diffuser exit pressure is finally computed from Equations 3.5 through 3.13. Note that the formation of a normal shock within the constant area section is still possible. The mixing pressure is updated using Equation 3.15 until satisfying the criterion of Equation 3.14.

3.2.2 Results

The previously described off-design model can be used to draw the characteristic curves of an ejector, given its geometry, stagnation conditions and efficiencies. Figure 3.1 shows the characteristic curves obtained using air as working fluid and assuming that the friction against the wall of the ejector can be neglected.

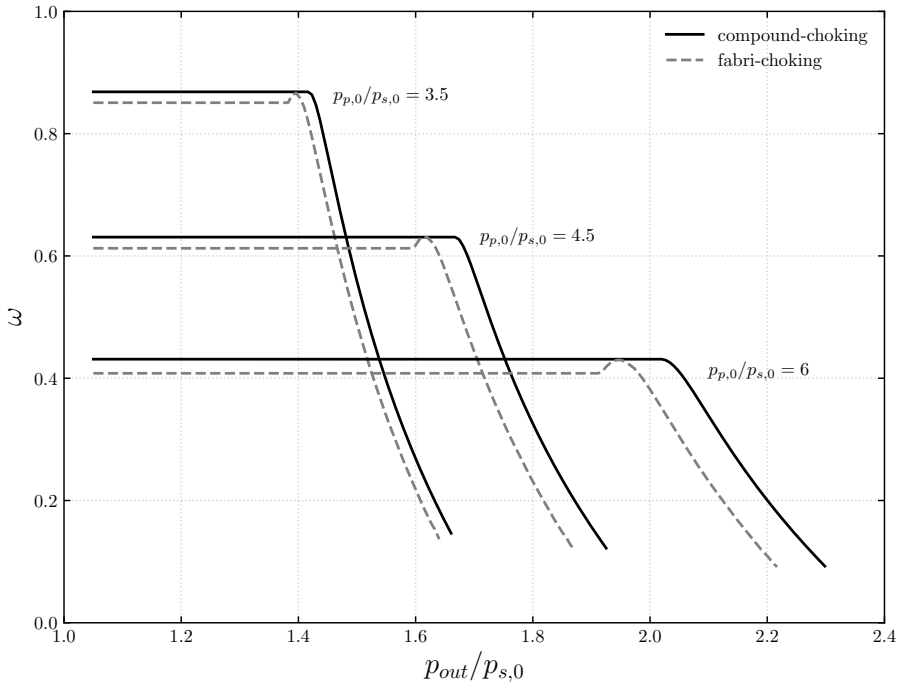

Figure 3.1: Characteristic curves obtained for air with the geometry shown in Figure 3.2. Friction is neglected at the wall and $\psi_m = 0.92$. Both choking criteria are represented.

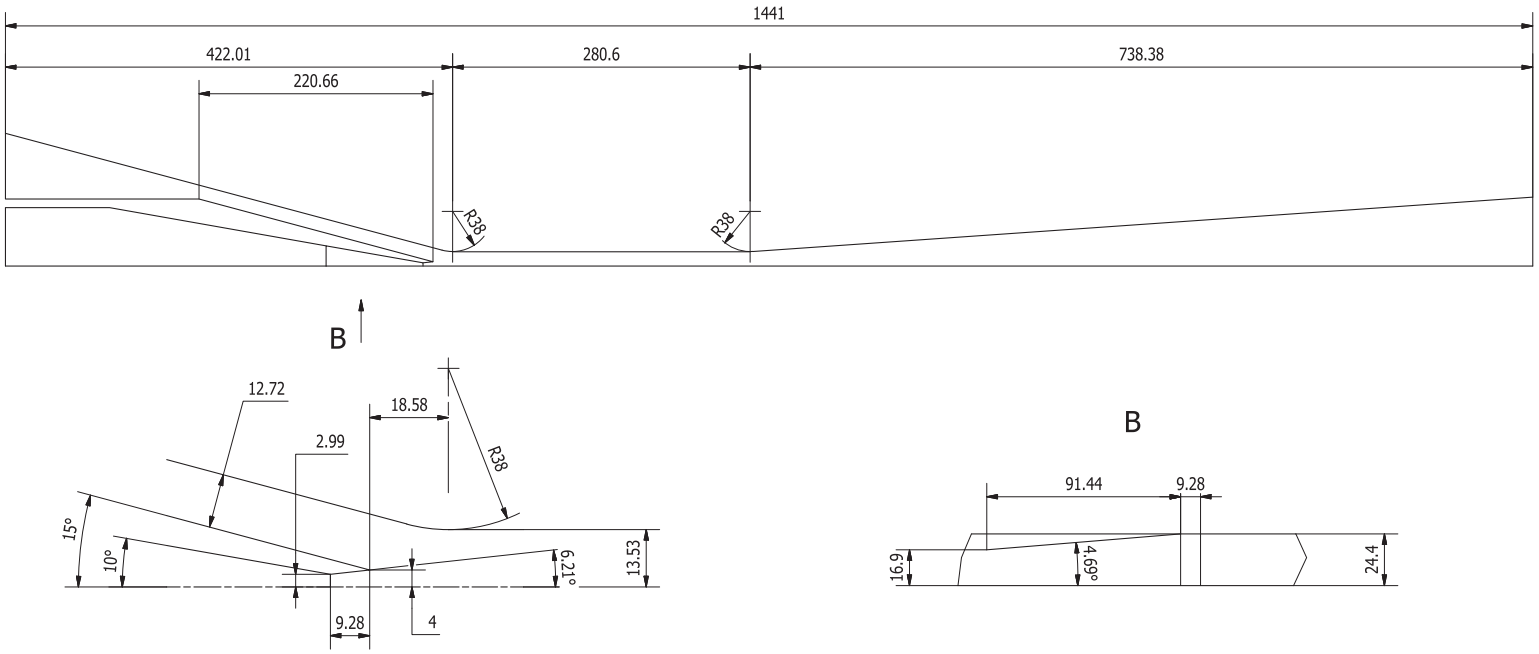

Figure 3.2: Dimensions of the air ejector that is modelled for the numerical computations and used to obtain the forthcoming experimental results [25].

Only the mixing efficiency η_m is not set to 1, with the constant factor ψ_m set to a value of 0.92. Figure 3.2 shows the dimensions that were used. Those dimensions correspond to the geometry of the air ejector that is available at UCLouvain, and were chosen here to allow easy comparison with the forthcoming results. This ejector has a rectangular cross section with an area ratio A_y/A_t of about 4.5.

One can observe in Figure 3.1 that the use of the compound-choking criterion systematically leads to a higher value of the entrainment ratio. Moreover, the use of the Fabri-choking criterion leads to an increase of the entrainment ratio for back pressures slightly higher than the critical pressure. It then reaches a maximum value and monotonically decreases. More interestingly, said maximum entrainment ratio is equal to the on-design entrainment ratio obtained using the compound-choking criterion. The fact that both models are equal a that point makes sense. Indeed, given the fact that the mixing pressure p_y obtained using the Fabri-choking criterion is inferior to that of the compound-choking criterion, increasing said pressure will eventually lead it to reach the value obtained using the compound-choking criterion.

One can also see that the off-design parts of the curves are not identical wether one uses the Fabri-choking or the compound-choking criterion. This is due to the fact that the critical pressures are different. Hence, the linear mixing efficiency η_m as expressed in Equation 3.16 will be different, and so will be state m, and therefore states 2 and d.

The phenomenology leading to the apparition of the local maximum in the off-design portion of the characteristic curve using the Fabri-choking criterion will be thoroughly detailed in a later section. Note however at this point that the curve obtained using the compound-choking criterion does not contain bump in off-design regime.

3.2.3 Conservation of mass

The previously described model, using either choking criteria and as described in the original article of Chen et al. [12], contains a major flaw. Indeed, the conservation of mass is not satisfied throughout the ejector. More precisely, because it is assumed that the mixing process between primary and secondary flows occurs at constant pressure (i.e. $p_y = p_m$), state m (cfr. Figure 2.1) can be fully defined without having to use the mass conservation equation. Because the mass conservation equation is not used, nothing constraints the mass flux to be conserved, so that :

$$\dot{m}_m \neq \dot{m}_p + \dot{m}_s \tag{3.17}$$

where $\dot{m}_m$ is the total mass flux at section m, i.e. when the two flows are fully mixed. This is a problem, as the point of a thermodynamic model is to predict ejector performance on

the basis of fundamental physical principles, including the conservation of mass. If the mass is not conserved, the model is not really more credible than a simple curve fitting.

3.3 New off-design model

In the previous section, an off-design model was described to predict ejector performance. However, the model did not conserve mass along the ejector. In this section, it is proposed to solve this problem. The final off-design model will be presented. Finally, a thorough analysis of the link between the Fabri-choking and the compound choking criteria will be performed.

3.3.1 Corrected model

To ensure the conservation of mass after mixing, the assumption of constant mixing pressure – i.e. Equation 3.2 – is lifted and replaced by the mass conservation equation. This also implies that an additional term is to be added to the momentum conservation equation, to take into account the pressure difference between sections m and y. This involves that state m has to be solved using an iterative method, as V_m depends on the unknown pressure p_m. State m is therefore defined by four equations. First, the conservation of mass :

$$\rho_m V_m A_y = \dot{m}_p + \dot{m}_s \tag{3.18}$$

Then, the momentum conservation equation :

$$V_m = \eta_m \frac{\dot{m}_p V_{p,y} + \dot{m}_s V_{s,y} + (p_y - p_m) A_y}{\dot{m}_p + \dot{m}_s} \tag{3.19}$$

Note at this point that η_m does not need to be a linear function of p_{out} as it was the case for the model of Chen et al. [12]. It will here be chosen as a constant : $\eta_m = \psi_m$. The third equation is the total enthalpy conservation equation given by Equation 3.4, and the last equation is the equation of state linking ρ_m, p_m and h_m :

$$\rho_m = \rho(p_m, h_m) \tag{3.20}$$

To solve this system of equations, the pressure p_m is guessed. The flow velocity V_m is then computed from Equation 3.19, along with the enthalpy h_m using Equation 3.4. The flow density ρ_m can then be obtained from Equation 3.20. The pressure p_m is then modified until Equation 3.18 is satisfied. More precisely, the solution is found using the same minimisation algorithm described in the previous chapter to find β. As a reminder, this efficient method to find the solution consists in restraining at each iteration the solution interval on p_m until finding the minimum of $|\rho_m V_m A_y - (\dot{m}_p + \dot{m}_s)|$.

With knowledge of state m, state 2 and d can be computed using Equations 3.5 through 3.13. Figure 3.3 summarises the computation algorithm of the new off-design model.

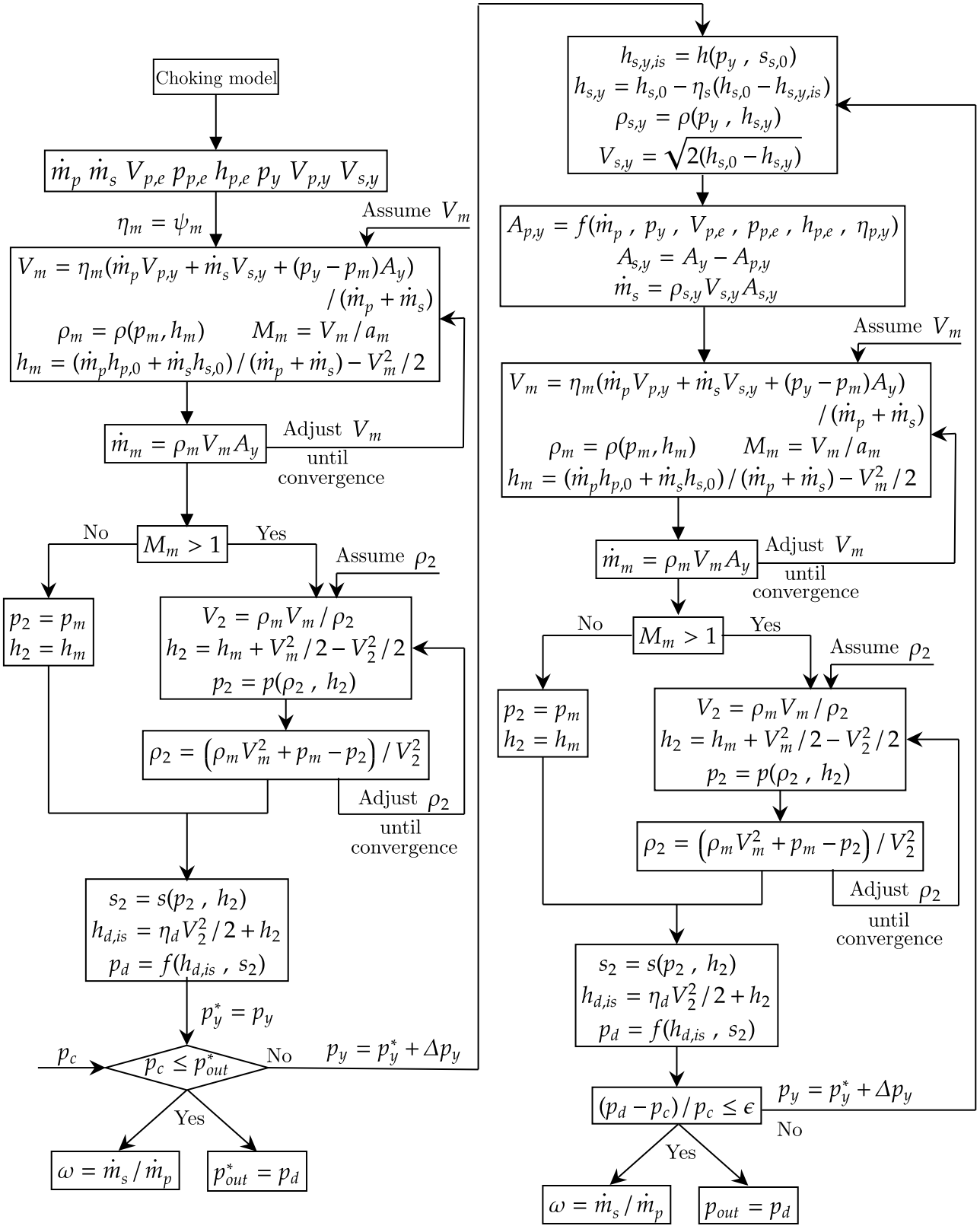

Figure 3.3: Flowchart of the model for off-design operation (cfr. Figure 2.1).

3.3.2 Results

Using the corrected set of equations previously described, one can once again draw the characteristic curves for air (cfr. Figure 3.4). As before, only the mixing efficiency is not set to 1. Again, this new model does not require for the mixing efficiency η_m to be a linear function of the back pressure. Instead, it can be set to a constant value (in this case $\eta_m = 0.92$), and the effect of the pressure difference between sections y and m will naturally tend to decrease the entrainment ratio as the back pressure gets higher. This makes more senses than the dynamic efficiency introduced by Chen et al. [12], as the latter would reach extremely low values for small entrainment ratios, that are not really representative of the mixing phenomena. In the present model, the entrainment ratio is rather limited by pressure effects.

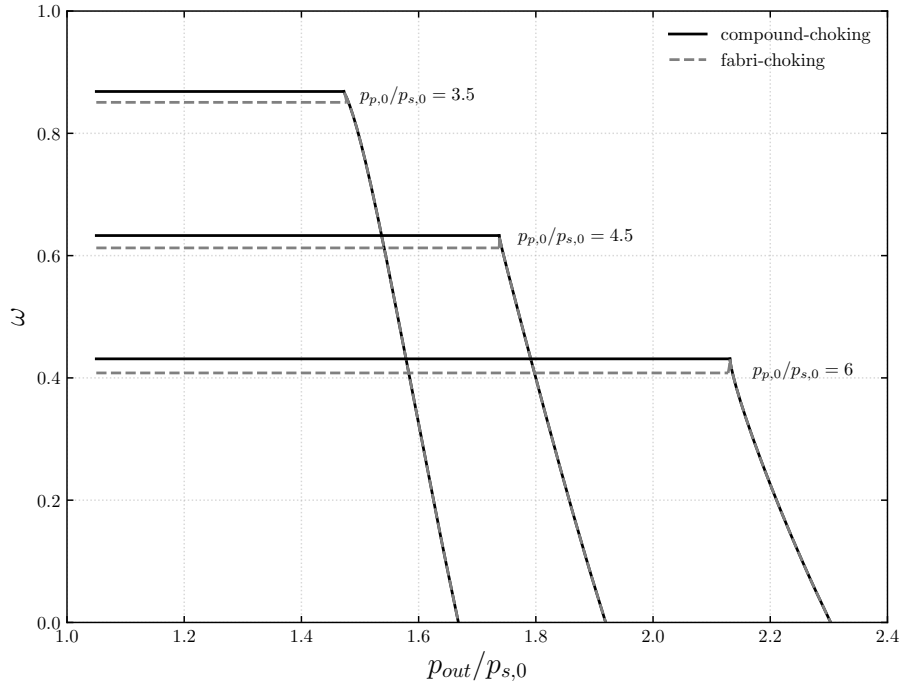

Figure 3.4: Characteristic curves obtained for air with the geometry shown in Figure 3.2. Friction is neglected at the wall and $\eta_m = 0.92$. Both choking criteria are represented.

One can observe in Figure 3.4 that the on-design plateau is at the same value than it was when using the faulty model. Again, this is because the on-design value of ω does not depend on sections m through d. However, the critical back pressure p^*_{out} is slightly higher for the corrected model. In addition, note that this time, the off-design part of the curves superimpose for Fabri and compound-choking. This comes from the fact that the mixing efficiency η_m is now independent of the back pressure. Therefore, the off-design

portions of the curves are computed in the exact same way, whichever choking criterion is used.

Much as seen before, the Fabri-choking criterion systematically predicts a lower on-design entrainment ratio. The off-design portion of the curve near the vicinity of the critical point is less obvious. Figure 3.5 shows a magnified view of the characteristic curve of Figure 3.4 for $p_{p,0}/p_{s,0} = 4.5$ around the critical point. The arrows along the off design part of the Fabri-choking curve indicate the direction along which p_y is increased. Hence, starting from the critical point of the Fabri-choking curve, increasing the pressure p_y leads the entrainment ratio to get higher, until it reaches the critical point associated to the compound-choking curve. At said critical point, the two curves merge and are indistinguishable.

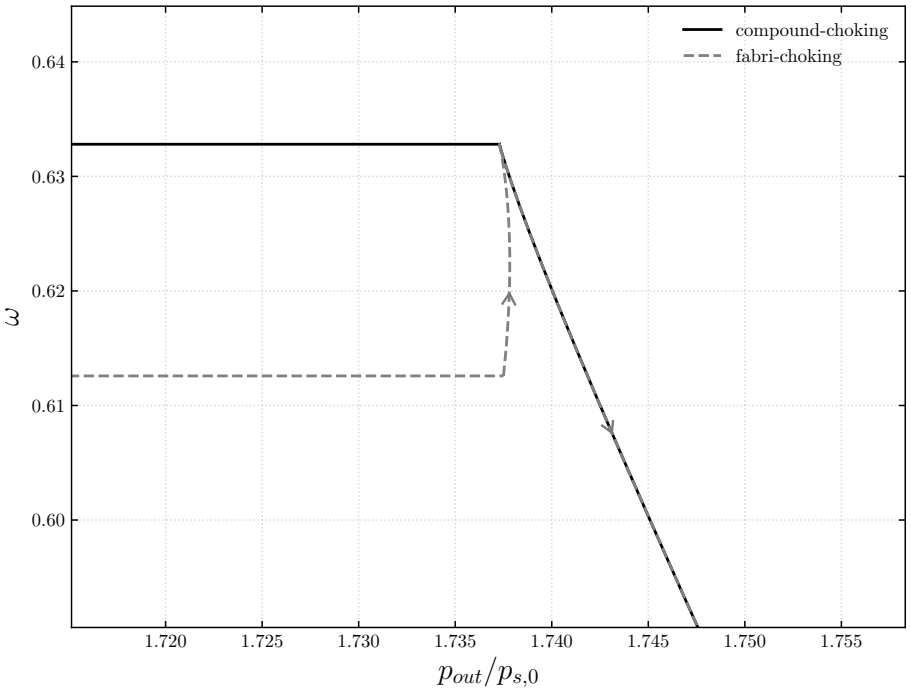

Figure 3.5: Magnified view of the characteristic curve of Figure 3.4 for $p_{p,0}/p_{s,0} = 4.5$ around the critical point.

Depending on the operating conditions, the critical pressure of the Fabri-choking curve might be higher or lower than that of the compound-choking curve. In the present case, the two critical pressures are extremely close. The junction from the Fabri to the compound-choking curve appears to be slightly cambered, so that p_{out} gets higher before decreasing to reach the critical pressure of the compound-choking curve. This phenomenon will be further discussed in the following chapter.

3.3.3 Link between Fabri-choking and compound-choking

It is now proposed to explain in more details the link between Fabri-choking compound-choking. To do that, the characteristic curves of Figure 3.4 for $p_{p,0}/p_{s,0} = 4.5$ are considered. As a reminder, those curves were obtained for air with $\eta_m = 0.92$. First, one can trace the evolution of the mixing pressure as a function of the back pressure (cfr. Figure 3.6). As mentioned previously, the design mixing pressure p_y^* is higher when using the compound-choking criterion. In addition, note that as the back pressure tends to the breakdown pressure, the mixing pressure tends to reach the secondary stagnation pressure. This makes sense, as when $p_y = p_{s,0}$, there is no pressure gradient to expand the secondary flow, hence $\dot{m}_s = 0$ and the entrainment ratio is zero.

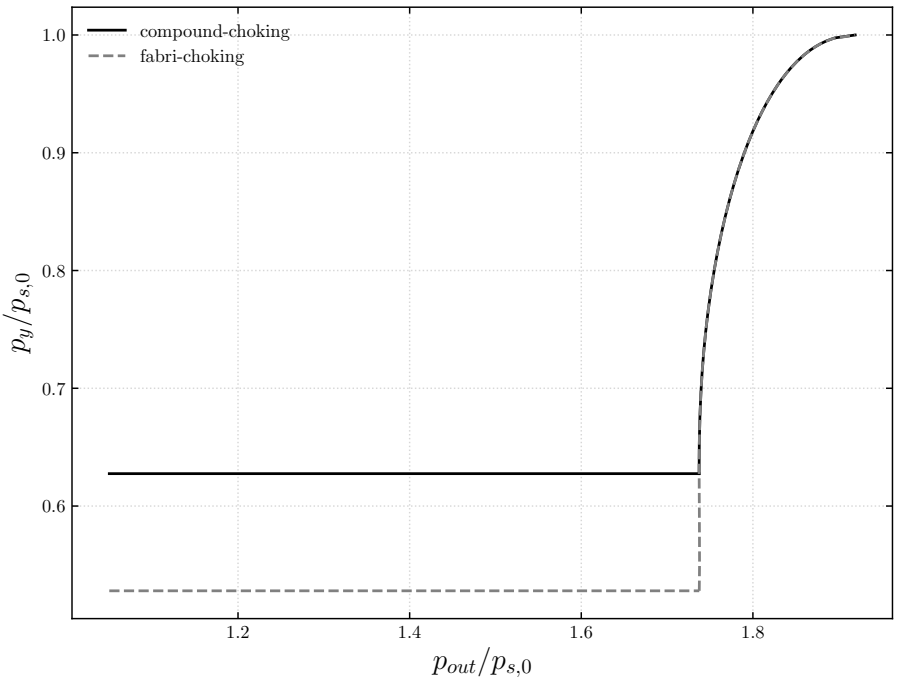

Figure 3.6: Mixing pressure as a function of the back pressure for $p_{p,0}/p_{s,0} = 4.5$. The working fluid is air and $\eta_m = 0.92$.

Then, one can trace the evolution of the entrainment ratio when the mixing pressure is increased (cfr. Figure 3.7). As a reminder, ω can be computed as a function of the mixing pressure and the stagnation conditions. Then, the positions of the critical conditions can be located for both choking criteria. Those are represented by dots on the curve. One can now clearly see why the compound-choking criterion systematically predicts higher entraiment ratios than the Fabri-choking criterion. Indeed, the entrainment ratio predicted by the compound-choking is located exactly at the maximum of the curve. This

means that considering isentropic flows, satisfying the compound-choking criterion will lead to the maximisation of the total mass flow rate within the ejector. Indeed, since the primary flow is choked, maximising ω is equivalent to maximising $\dot{m}_s$ and therefore $\dot{m}_p + \dot{m}_s$.

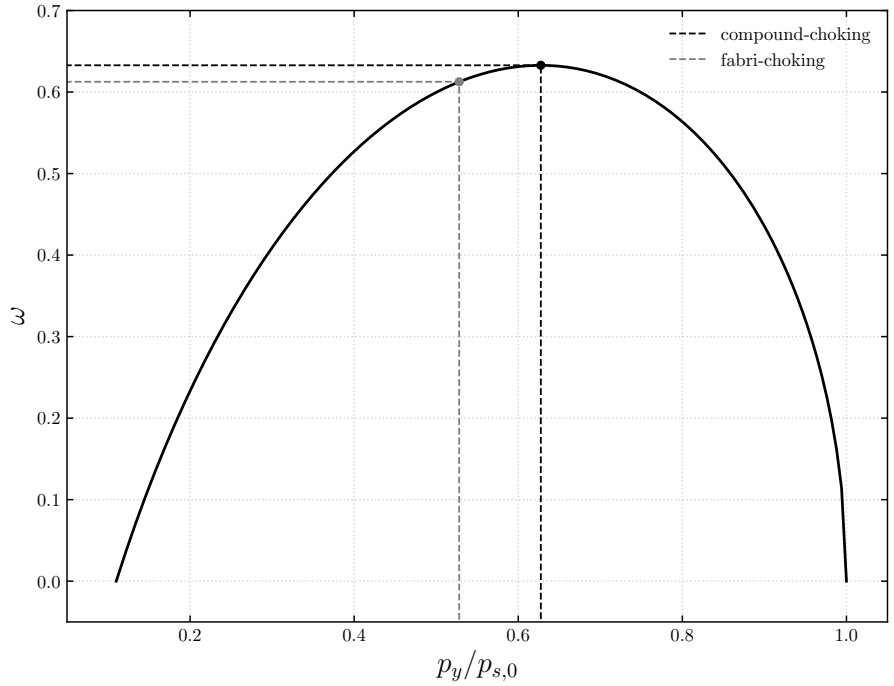

Figure 3.7: Entrainment ratio as a function of the mixing pressure for $p_{p,0}/p_{s,0} = 4.5$. The working fluid is air and $\eta_m = 0.92$. The position of the critical conditions have been highlighted.

On the other hand, the Fabri-choking mixing pressure at critical conditions p_y^* is slightly lower than the that of the maximum. This explains why the off-design part of the Fabri-choking characteristic curve connects with the compound-choking characteristic curve at the critical point as p_y increases. This also explains why the Fabri-choking criterion predicts that the entrainment ratio will increase before decreasing as the back pressure gets raised.

3.4 Conclusion

In this chapter, the off-design part of the thermodynamic model was described. First, the off-design model of Chen et al. [12] was presented and yielded promising results,

as well as a clarification on the differences between the Fabri-choking criterion and the compound-choking criterion. The characteristic curves for an air ejector with negligible wall friction were traced. However, this initial model was found to be flawed, as the mass flux was not conserved throughout the ejector.

A new off-design model was proposed, with corrections that ensured mass conservation. This new model was found to provide somewhat similar results, with the advantage that it does not require to consider a mixing efficiency that is linearly dependant on the back pressure, as for the model of Chen et al. [12]. This leads to the fact that both choking criteria converge for off-design operation.

Lastly, the link between Fabri-choking and compound-choking was investigated. It was found that the compound-choking criterion leads to a maximisation of the total mass flux within the ejector for isentropic flows, therefore systematically leading to higher predictions of the entrainment ratio. The Fabri-choking criterion maximises primary and secondary flows separately, therefore leading to lower predictions. This may lead to believe that the compound-choking criterion might be more appropriate to describe ejector flows, as it predicts the physically highest mass flow rate allowable within the ejector. This could be seen as an extension of the definition of choking for classical nozzles to ejectors.

CHAPTER 4

Calibration of the model

4.1 Introduction

In this chapter, it is proposed to calibrate the previously described model in order to fit experimental data. The purpose is to be able to predict ejector performance for any operating conditions, without having to perform expensive CFD computations or additional experiments. The calibrated thermodynamic model would therefore allow to design ejectors quite quickly. The calibration will be performed by means of the isentropic and mixing efficiencies previously defined. First, the individual impact of each efficiency will be investigated. Then, the model will be calibrated for R134a ejectors, as well as for the air ejector available at UCLouvain. The impact of friction on the compound-choking criterion will be the subject of the last section.

4.2 Impact of the efficiencies

In order to efficiently perform the calibration operation, it is relevant to assess the individual effect of each of the efficiencies on the shape of the characteristic curves. To do this, multiple characteristic curves are drawn, by varying one of the efficiencies. Figures 4.1 through 4.5 show the impact of the four isentropic efficiencies (i.e. η_p, η_s, $\eta_{p,y}$ and η_d) and the mixing efficiency η_m. Note that by default, the isentropic efficiencies are set to 1 and η_m to 0.95.

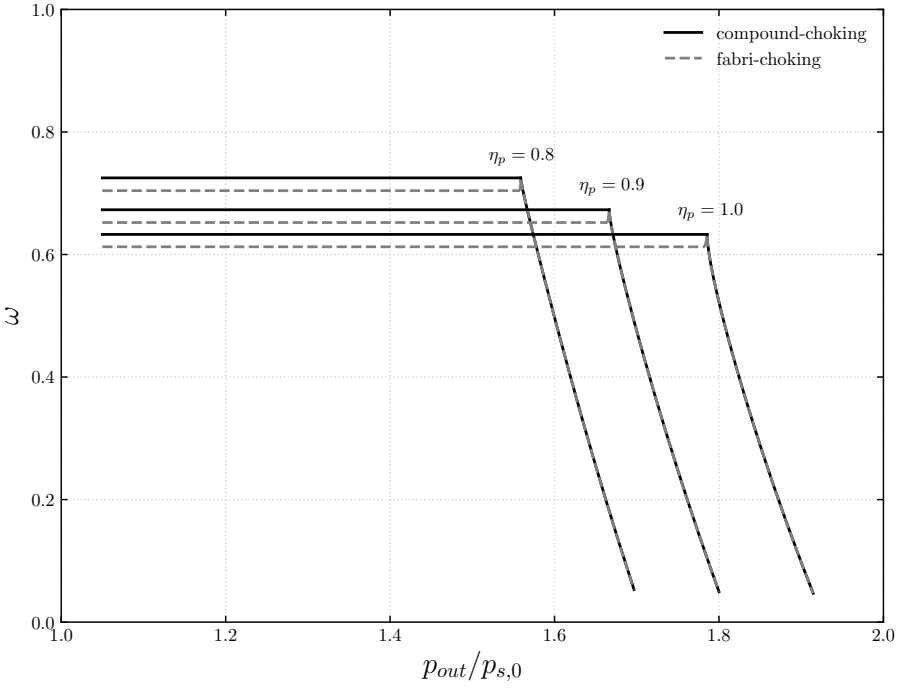

Figure 4.1: Impact of η_p on the characteristic curves.

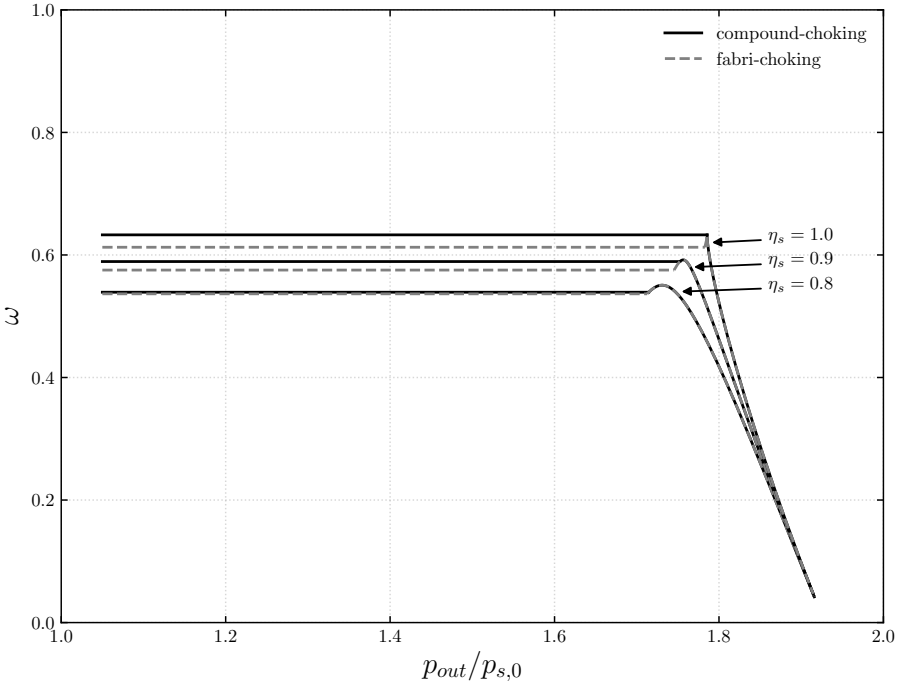

Figure 4.2: Impact of η_s on the characteristic curves.

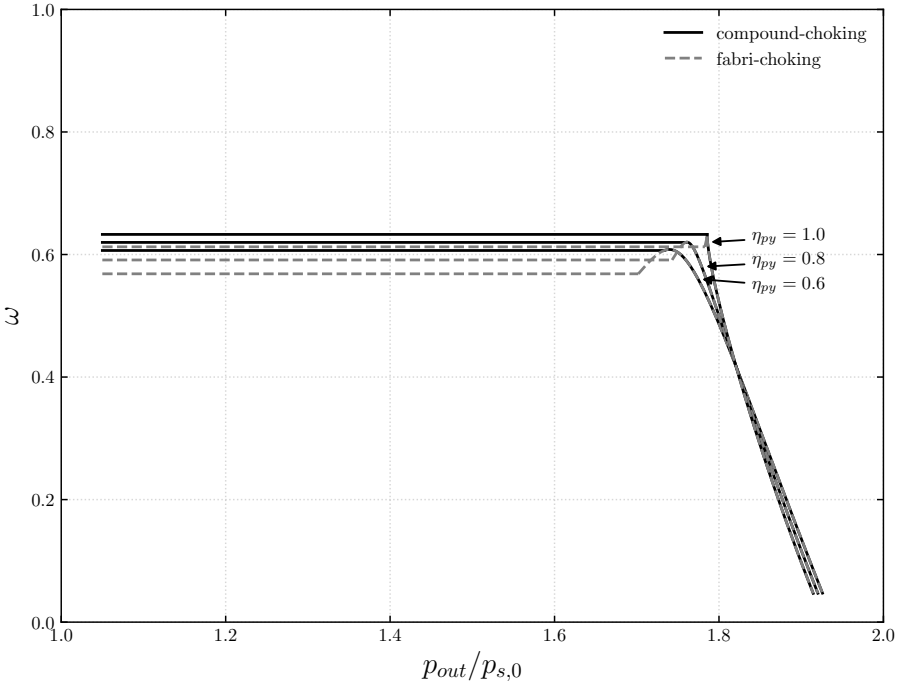

Figure 4.3: Impact of $\eta_{p,y}$ on the characteristic curves.

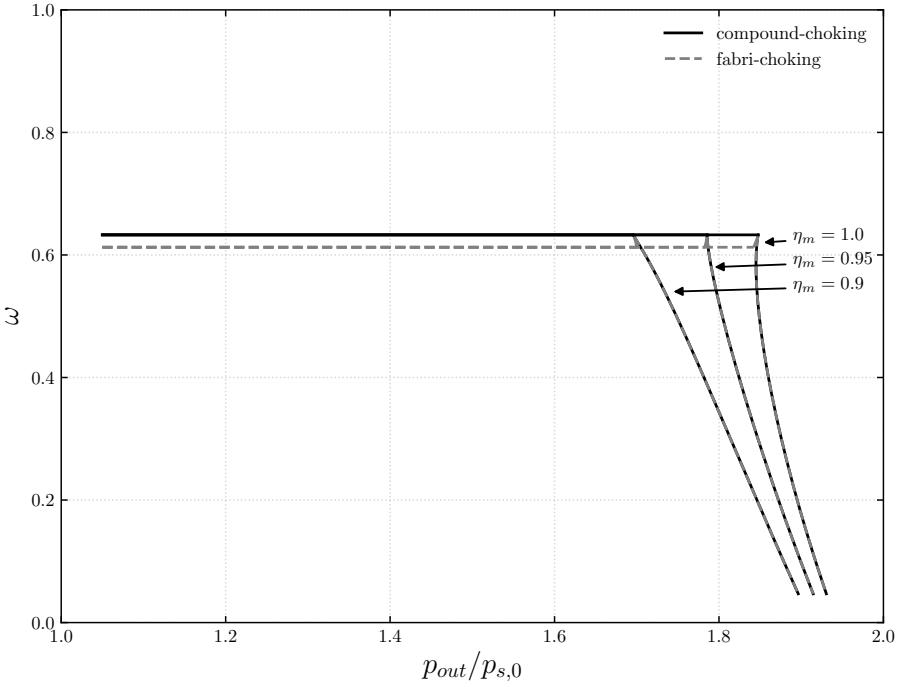

Figure 4.4: Impact of η_m on the characteristic curves.

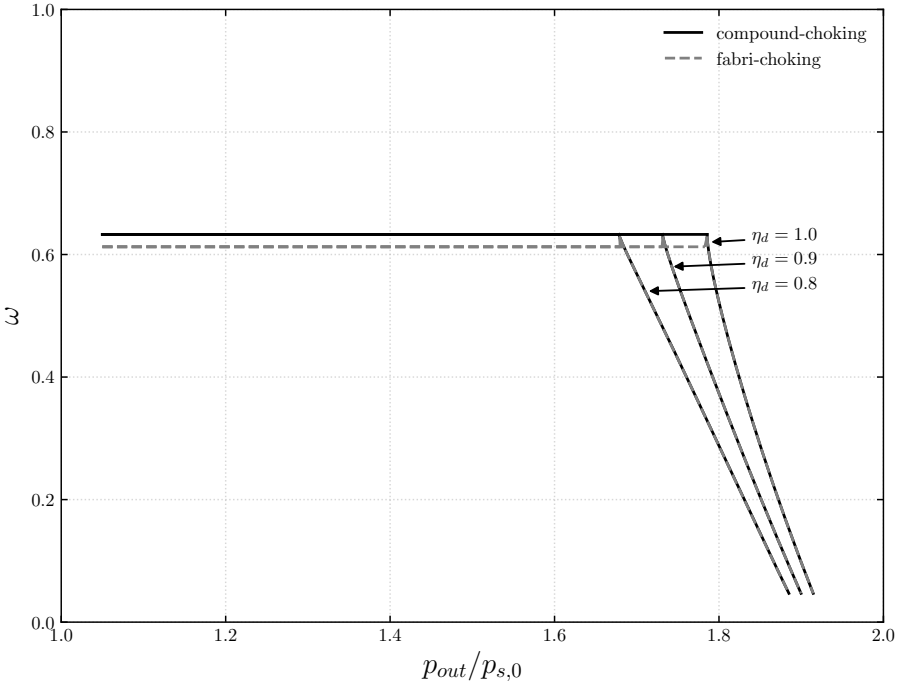

Figure 4.5: Impact of η_d on the characteristic curves.

One can determine the influence of the different efficiencies :

- η_p : As η_p gets lower, the primary mass flow rate is decreased, as the flow velocity at the primary throat gets lower. The on-design entrainment ratio therefore increases. The effect of friction in the primary nozzle is somewhat equivalent to having a lower primary stagnation pressure. This explains the fact that the critical back pressure gets lower. The curves behaviour as η_p decreases is reminiscent of that of the curves drawn in Figure 3.4.
- η_s : As η_s gets lower, the on-design entrainment ratio gets lower, as the secondary mass flow rate is decreased. The back pressure is closely related to the total mass flux going through the ejector. Thus, a lower secondary mass flow rate also results in a decrease of the critical back pressure. Note also that the off-design curves all have the same breakdown pressure. This is explained by the fact that at the breakdown pressure, $\dot{m}_s = 0$ and the secondary flow does not influence the total flow anymore. This is not true when η_p varies, which is why the breakdown pressures in Figure 4.1 are not the same. Moreover, one can observe that the same bump that was previously observed only for Fabri-choking curves is now also present on the compound-choking curves. This will be further explained in a following section.
- $\eta_{p,y}$: Decreasing $\eta_{p,y}$ has a somewhat similar effect to decreasing η_s, but to a lesser extent. However, none of the two mass fluxes are directly hindered by this

efficiency. As $\eta_{p,y}$ gets lower, the primary flow is expanded less efficiently in the mixing chamber. The friction hinders the primary flow expansion (as the primary flow is supersonic), so that the primary flow mixing area $A_{p,y}$ gets higher. Conversely, the secondary flow mixing area $A_{s,y}$ gets lower, therefore decreasing the secondary mass flux.

- η_m : Lowering η_m does not influence the on-design entrainment ratio, as the latter does not depend on mixing phenomena. As η_m decreases, the critical back pressure decreases. Indeed, assuming that the mixed flow is at subsonic speed, the friction interactions will tend to accelerate the flow, thereby lowering the back pressure. This is comparable to a Fanno flow. Notice also the shape of the off-design curve for $\eta_m = 1$. This curve is slightly cambered towards the left, meaning that as the mixing pressure p_y gets higher, the back pressure effectively decreases before increasing again. This case actually constitutes a limitation of the model. This inversion in the evolution of p_{out} as p_y gets higher can be traced back to an inversion of the entropy s_2 (cfr. Equation 3.10) as p_y gets higher. The entropy s_2 should be monotonically decreasing as p_y is raised. In fact, in the inversion zone, a shock is modeled by Equations 3.4, 3.19 and 3.20 at section m, meaning that $V_m < V_{s,y} < V_{p,y}$. This explains the unexpected increase in entropy in the inversion region. However, for real ejectors, the transition from on to off-design should be done smoothly, and this inversion would lead to a discontinuity as the back pressure is raised from p^*_{out}.
- η_d : The effect of η_d is quite similar to that of η_m. Lowering η_d will tend to decrease the critical back pressure.

It was chosen not to use the diffuser isentropic efficiency η_d for later calibration. Indeed, this efficiency has the same influence on the characteristic curves as η_m. Furthermore, in real ejectors, the diffuser is usually well designed, meaning that it can reasonably be assumed that the flow is isentropic. In addition, it was chosen to use the compound-choking criterion for the following results.

4.3 R134a ejectors

To calibrate the characteristic curves for R134a ejectors, the experimental data of Garcia del Valle et al. [15] were used as reference. Three different geometries were presented in the original article. However, they differ only in shape ; the areas at the sections of interest are equal. For this reason, only one ejector can be modeled using the present 0-D model. The geometry of said ejector is shown in Figure 4.6.

It was found that an accurate calibration could be performed by using only three parameters, that are, $\eta_p = 0.977$, $\eta_s = 0.89$ and $\eta_m = 0.813$. The value of $\eta_{p,y}$ is thus maintained to

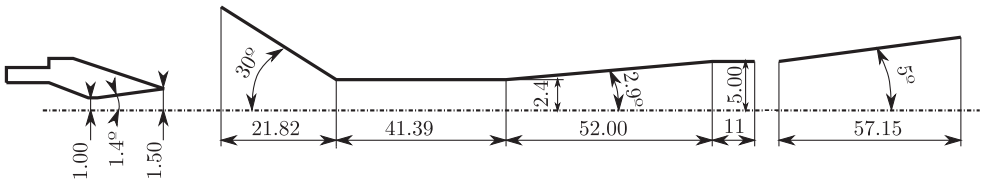

Figure 4.6: Dimensions of the R134a ejector used for the calibration. All dimensions are in [mm]. This corresponds to geometry A in [15].

1. Note that the values chosen for the efficiencies appear to be plausible for real ejectors. Indeed, the primary nozzle flow is almost isentropic and the secondary flow slightly less due to the more complex geometry. The most limiting factor is the mixing efficiency. In addition, it was not necessary to introduce a linear function of the back pressure for η_m in order to match the off-design curve slope. The stagnation conditions for this operating point are $(T_{sat})_{p,0} = 84.38°\text{C}$ and $(T_{sat})_{s,0} = 10°\text{C}$ with a superheating of 10°C. Superheating the vapour ensures that the flow will not condense within the ejector.

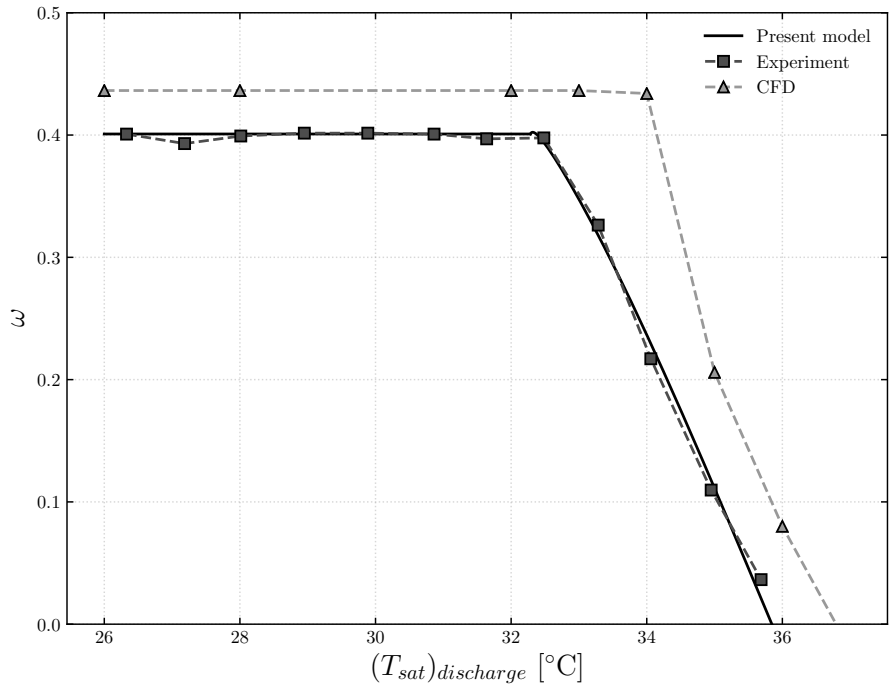

Figure 4.7: Characteristic curve obtained for the geometry of Garcia del Valle et al. [15] with $(T_{sat})_{p,0} = 84.38°C$, $(T_{sat})_{s,0} = 10°C$, $\eta_p = 0.977$, $\eta_s = 0.89$ and $\eta_m = 0.813$.

Figure 4.7 shows the results of the calibration, along with CFD results obtained by researchers at the University of Sherbrooke [29]. The model fits quite well the experimental data of Garcia del Valle et al. [15], even better than the CFD results that tend to overestimate the entrainment ratio.

	Ejector I	Ejector II	Ejector III
Primary pressure $p_{p,0}$ [kPa]	2900	2633	1934
Primary temperature $T_{p,0}$ [°C]	106	100	86
Secondary pressure $p_{s,0}$ [kPa]	265	350	415
Secondary temperature $T_{s,0}$ [°C]	50	25	30
Primary throat diameter D_t [mm]	5.63	7.09	8.03
Primary nozzle exit diameter D_e [mm]	7.85	9.70	11.35
Mixing section diameter D_y [mm]	16.4	16.4	16.4

Table 4.1: Geometry and operating conditions for the three experiments of Hakkaki-Fard et al. [18].

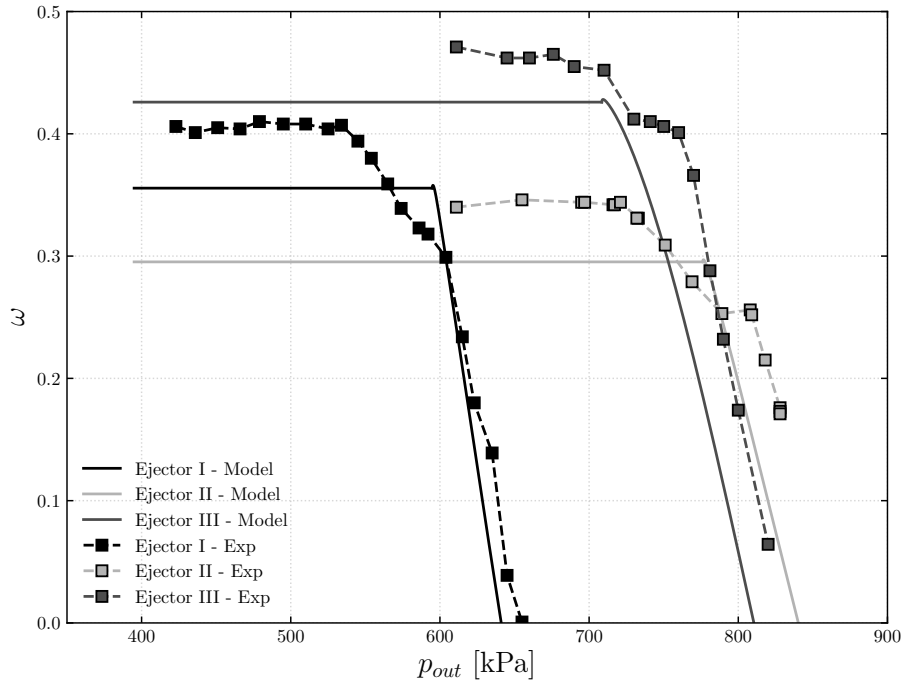

Figure 4.8: Characteristic curves obtained for the ejectors of Hakkaki-Fard et al. [18] with $\eta_p = 0.977$, $\eta_s = 0.89$ and $\eta_m = 0.813$.

Using the calibration parameters found for the ejector of Garcia del Valle et al. [15], one can draw the characteristic curves for other R134a ejectors to see if the calibration stays

accurate. It was chosen to consider the ejectors of Hakkaki-Fard et al. [18]. The three ejector geometries and operating conditions that were tested experimentally are summarised in Table 4.1.

Figure 4.8 shows the results of the fitting for the three ejectors. One can observe that although the model does not predict the entrainment ratio as accurately as for the ejector of Garcia del Valle et al. [15], it nevertheless gives a good approximation. The model appears to underestimate the on-design entrainment ratio, but the off-design part of the characteristic curves seem to fit quite nicely. More precisely, the slopes of the off-design curves are quite accurate, and the model even overlaps the experiment for Ejector I. One could argue that the calibration process should yield better results if it were performed on one of the ejectors of Hakkaki-Fard et al. However, by doing so, the predictions of the characteristic curves for the two other ejectors were found to be quite poor. Using the parameters found for the ejector of Garcia del Valle et al. was observed to yield the overall best predictions for the three ejectors of Hakkaki-Fard et al.

4.4 Air ejectors

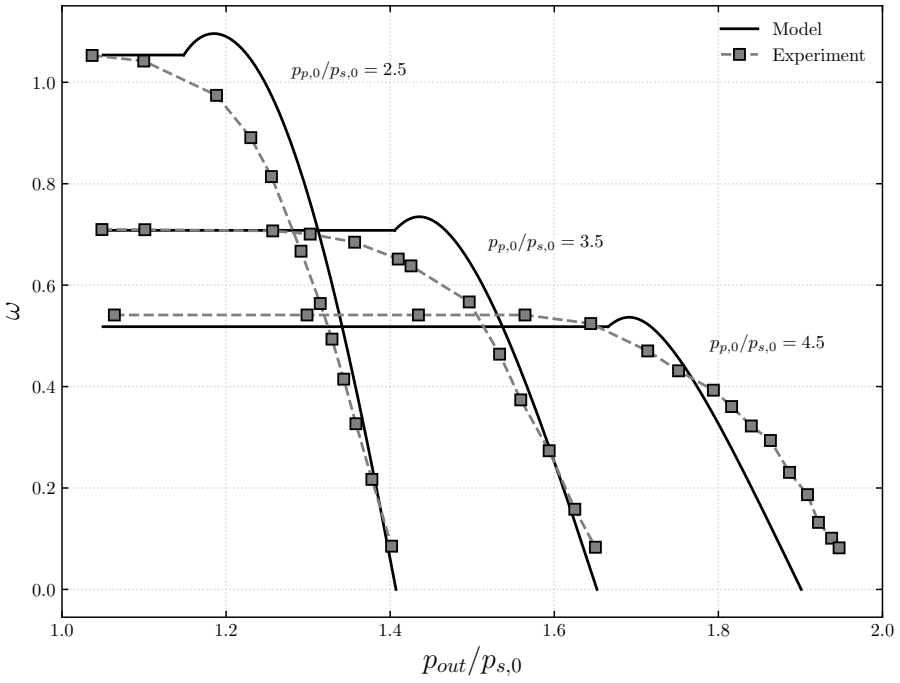

Figure 4.9: Characteristic curves obtained for the air ejector available at UCLouvain with $\eta_p = 0.977$, $\eta_s = 0.75$ and $\eta_m = 0.95$.

The model was also calibrated on the experimental data obtained from the air ejector

available at UCLouvain. As a reminder, the geometry of said ejector is given in Figure 3.2. Again, the calibration could be performed by means of only three parameters, that are, $\eta_{p,y} = 0.977$, $\eta_s = 0.75$ and $\eta_m = 0.95$. As before, $\eta_{p,y}$ is set to 1.

Figure 4.9 shows the fitting results that were obtained by calibrating the parameters on the experimental data gathered for $p_{p,0}/p_{s,0} = 3.5$. Note that the secondary stagnation conditions correspond to the atmospheric ones for this particular ejector, so that $p_{s,0} = 1$ [bar]. One can see that the calibration allowed the model to fit relatively well the experimental curves for the three cases. The off-design slopes do however not match the experimental data as well as for the case of Garcia del Valle et al. [15] seen previously. The error remains however limited, and the general shape of the curves is relatively close to that of the experimental ones. The main issue with those curves is that there is a significant increase in the entrainment ratio right after the critical point. This will be the subject of the next section.

4.5 Non-isentropic compound-choking correction

As mentioned previously, if the ejector flow is non-isentropic, using the compound-choking criterion to produce the characteristic curves leads to the apparition of a bump in the off-design part of the curves. This actually makes sense because the compound-choking criterion as derived in the frame of this work relies on the assumption that both flows are isentropic between sections e and y. This means that applying the compound-choking criterion whilst allowing $\eta_s < 1$ leads to an error in the computation of the choking conditions. In other words the definition of β given in Equation 2.54 is not correct anymore.

Although it has not been analytically proven that the compound-choking criterion systematically maximises the mass flow rate within the ejector, this will here be taken as an assumption. In that case, the way to solve the problem actually becomes quite simple. If the mass flow rate – and therefore ω – is maximum at the choking conditions, one has only to define the critical point as the point at the top of the bump of the off-design part of the characteristic curve.

As was explained in the previous chapter, deriving a true expression for the compound-choking criterion for non-isentropic flows is out of the scope of this study. An alternative would be to define the compound-choking indicator β as a function of η_s, instead of imposing $\beta = 0$. Figure 4.10 shows the compound choking indicator as a function of η_s for ejector conditions leading to the maximisation of the total mass flow rate. The working fluid is air with $p_{p,0}/p_{s,0} = 3.5$, $\eta_m = 0.95$ and all other efficiencies set to 1. Note that

the plot is in semi-logarithmic scale. The curve defined by β can then easily be fitted by an analytical function. In this case, the shape of the curve is reminiscent of that of the tangent function. The fitting curve is therefore given by :

$$\beta = \beta_f \tan\left(-\frac{\pi}{2}(\eta_s + 1)\right) \tag{4.1}$$

with β_f the value taken by β at the inflection point, i.e. at $\eta_s = 0.5$.

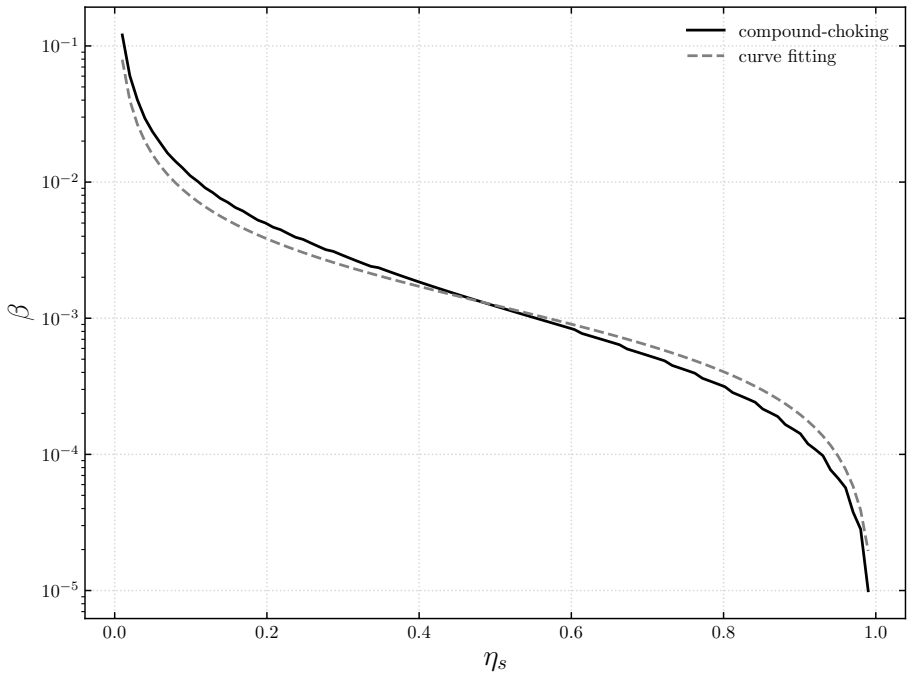

Figure 4.10: Compound choking indicator as a function of η_s for ejector conditions leading to the maximisation of the total mass flow rate.

One can observe in Figure 4.10 that β gets higher as η_s gets lower, and that it tends to zero as η_s tends to 1. Actually, when $\eta_s = 1$, β is exactly – up to the machine precision – equal to zero, as in this case the criterion $\beta = 0$ is analytically correct. Notice also that as η_s tends to zero, β tends to the infinity. The computation interval was in this case restrained to $[0.01; 0.99]$ for better visibility.

Using this new compound-choking criterion, the characteristic curves previously drawn can be corrected. For example, the curves for the air ejector of Figure 4.9 have been corrected and are shown in Figure 4.11. Note that in order to better fit the experimental data, η_s has been changed from 0.75 to 0.71. Such a low isentropic efficiency could be

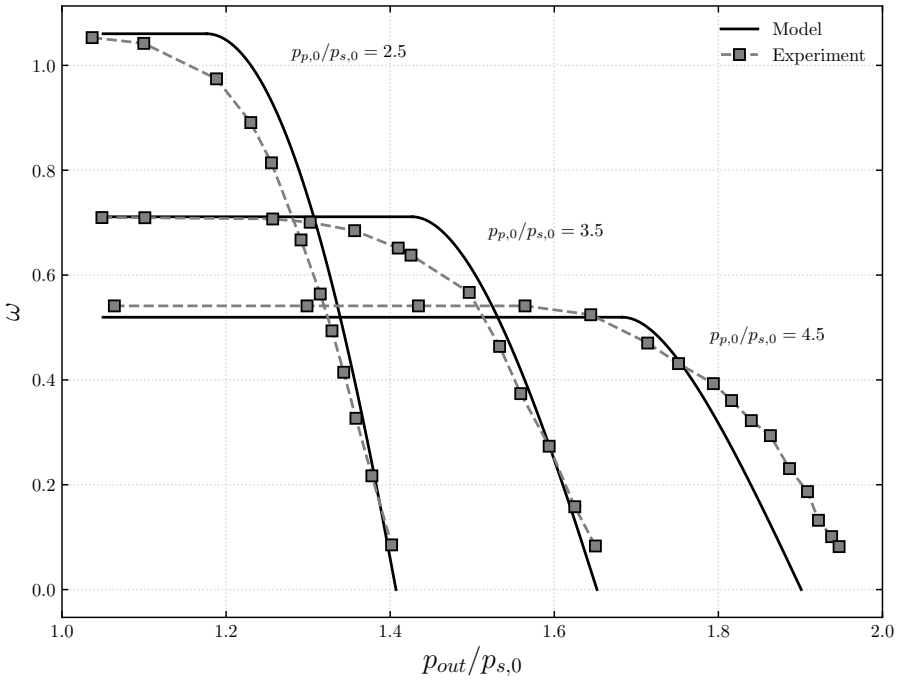

Figure 4.11: Corrected characteristic curves obtained for the air ejector available at UCLouvain with $\eta_p = 0.977$, $\eta_s = 0.71$ and $\eta_m = 0.95$.

explained by the fact that the air ejector geometry is quite complex. Indeed, the secondary flow has to turn from 90° at the inlet.

4.6 Conclusion

In this chapter, the different impacts of the five efficiencies introduced into the model were studied. It was then found that the calibration process could be performed in a satisfactory manner using only three parameters : η_p, η_s and η_m.

The calibration was first performed on R134a ejectors with the experimental data of Garcia del Valle et al. [15]. A quite accurate fitting of the model was found to be possible. Keeping the same calibration parameters, the model was then used to predict the performance of the three ejectors of Hakkaki-Fard et al. [18]. The predictions were found to be less accurate than for the case of Garcia del Valle et al., but a good correlation of the model with the experimental data was nevertheless ensured.

Then, the model was calibrated on the experimental data obtained from the air ejector

available at UCLouvain. Despite the particular geometry of said ejector, a good fitting of the data was found to be possible.

Lastly, an empirical correction was proposed to the compound-choking criterion for non-isentropic flows. This correction consists in assuming that the compound-choking criterion leads to the maximisation of the total mass flow rate within the ejector, whether or not the flow is isentropic.

CHAPTER 5

Conclusion

5.1 Achievements

Ejector design remains to this day a particular challenge due to the inherent difficulty to predict ejector performance. Thermodynamic models allow for swift predictions, which is why they are abundant in the literature. In this work, a new real gas thermodynamic model was developed. This model can predict ejector performance for single or two-phase flows and be calibrated by means of multiple efficiencies.

First, a modified version of the model of Chen et al. [12] was implemented. Two on-design models were described, that differ in the choking criterion that was applied. The first model, that used the Fabri-choking criterion, was found to perform quite poorly when compared to the experimental data of Huang et al. [20]. The second model, that used the compound-choking criterion derived from the theory of Bernstein et al. [7], yielded much better predictions, with most predictions within 10% error from the experimental data.

Then, the off-design part of the model of Chen et al. was implemented. However, this model was found to be flawed, as the mass was not conserved throughout the ejector. A new model was subsequently proposed to solve this issue. In particular, the assumption of constant mixing pressure has been lifted, which allowed the introduction of the mass conservation equation back into the model. The decrease in performance in off-design regime was thereby modeled by pressure effects within the constant area duct. The new off-design model was then used to perform an analysis on the connections between Fabri-choking and compound-choking. It was found that the use of the compound-choking criterion leads to the maximisation of the total mass flow rate within the ejector, whereas the Fabri-choking criterion tends to underestimate it.

The individual impact of each calibration parameter was then investigated. The new model was calibrated, using the compound-choking criterion, with experimental data for R134a and air ejectors. A good fitting ability was found to be possible for both fluids by using only three fitting parameters. In addition, it was not required to use a dynamic mixing efficiency, as it was the case in the original model of Chen et al. [12]. Lastly, an empirical correction was proposed to the compound-choking criterion for non-isentropic flows.

The model derived in the present document, along with the connections between compound-choking and Fabri-choking, will be published as part of an upcoming article.

5.2 Research perspectives

The most limiting assumption of this model is that the mixing process takes place within the constant area section. A possible improvement would be to lift that assumption, therefore considering the entire geometry of the ejector, instead of discrete sections. This would allow the mixing phenomena to take place within the mixing chamber with variable cross sectional area.

One could also consider implementing shock relations right at the exit of the primary nozzle, as can be experimentally observed. This may lead the primary flow to get to more appropriate conditions when the mixing phenomena start to occur. Likewise, removing the assumption of uniform pressure between primary and secondary flows at the mixing section might also lead to improved prediction abilities.

An additional improvement could be to provide an analytical demonstration that the compound-choking criterion indeed provides the maximum mass flow rate physically allowable within the ejector. Likewise, one could derive an expression for the compound-flow indicator that would take friction losses into account.

Lastly, one could further investigate the behaviour of the compound-choking indicator at the maximum mass flow conditions. An analysis could be made to shed light on the dependencies on the fluid, geometry, and operating conditions. This could allow to better fit the compound-choking indicator for flows with friction losses and therefore further improve the model.

APPENDIX A

Additional

A.1 Maximisation of the mass flow rate

In this appendix, it is proposed to demonstrate that in the case of an isentropic nozzle flow, maximising the mass flow rate per unit area is equivalent to imposing Mach unity at the throat.

The mass flow rate per unit area G can be expressed as :

$$G = \rho\, V, \tag{A.1}$$

with ρ the fluid density and V the flow velocity. When G is maximum, one has :

$$\left(\frac{\partial(\rho V)}{\partial p}\right)_s = V\left(\frac{\partial \rho}{\partial p}\right)_s + \rho\left(\frac{\partial V}{\partial p}\right)_s = 0. \tag{A.2}$$

From the definition of the speed of sound a, one has that :

$$\left(\frac{\partial \rho}{\partial p}\right)_s = \frac{1}{a^2}, \tag{A.3}$$

and from the conservation of total enthalpy :

$$\begin{aligned}\left(\frac{\partial V}{\partial p}\right)_s &= \left(\frac{\partial}{\partial p}\right)_s \left(\sqrt{2\,(h_0 - h)}\right) \\ &= -\frac{1}{\sqrt{2\,(h_0 - h)}}\left(\frac{\partial h}{\partial p}\right)_s \\ &= -\frac{1}{V}\left(\frac{\partial h}{\partial p}\right)_s,\end{aligned} \tag{A.4}$$

where h_0 is the total enthalpy. Injecting Equations A.3 and A.4 into Equation A.2 gives :

$$\frac{V^2}{a^2} = \rho \left(\frac{\partial h}{\partial p}\right)_s . \tag{A.5}$$

One can then use the Equation of Gibbs :

$$T\, ds = dh - \frac{1}{\rho} dp, \tag{A.6}$$

which re-writes, for isentropic transformations, into :

$$\left(\frac{\partial h}{\partial p}\right)_s = \frac{1}{\rho}. \tag{A.7}$$

Introducing the latter relation into Equation A.5 gives :

$$\frac{V^2}{a^2} = 1, \tag{A.8}$$

or, equivalently :

$$V = a. \tag{A.9}$$

This means that, assuming an isentropic expansion, the sonic conditions will be reached when the mass flux per unit area is maximum.

References

[1] Diagram of an ejector [digital image]. (© transvac 2018). retrieved from https://www.transvac.co.uk/howanejectorworks.php.

[2] Z. Aidoun, K. Ameur, M. Falsafioon, and B. Messaoud. Current advances in ejector modeling, experimentation and applications for refrigeration and heat pumps. part 1: Single-phase ejectors. *Inventions*, 4:15, 03 2019.

[3] Z. Aidoun, K. Ameur, M. Falsafioon, and B. Messaoud. Current advances in ejector modeling, experimentation and applications for refrigeration and heat pumps. part 2: Two-phase ejectors. *Inventions*, 4:16, 03 2019.

[4] F. Aligolzadeh and A. Hakkaki-Fard. A novel methodology for designing a multi-ejector refrigeration system. *Applied Thermal Engineering*, 151:26 – 37, 2019.

[5] N. H. Aly, A. Karameldin, and M. Shamloul. Modelling and simulation of steam jet ejectors. *Desalination*, 123(1):1 – 8, 1999.

[6] K. Ameur, Z. Aidoun, and M. Ouzzane. Modeling and numerical approach for the design and operation of two-phase ejectors. *Applied Thermal Engineering*, 109:809 – 818, 2016.

[7] A. Bernstein, W. H. Heiser, and C. Hevenor. Compound-Compressible Nozzle Flow. *Journal of Applied Mechanics*, 34(3):548–554, 09 1967.

[8] G. Besagni. Ejectors on the cutting edge: The past, the present and the perspective. *Energy*, 170:998 – 1003, 2019.

[9] G. Besagni, R. Mereu, and F. Inzoli. Ejector refrigeration: A comprehensive review. *Renewable and Sustainable Energy Reviews*, 53:373 – 407, 2016.

[10] A. Bouhanguel. *Etude numérique et expérimentale de l'interaction entre deux écoulements compressibles dans un éjecteur supersonique.* PhD thesis, Université de Franche-Comté, 2013.

[11] W. Chen, M. Liu, D. Chong, J. Yan, A. B. Little, and Y. Bartosiewicz. A 1d model to predict ejector performance at critical and sub-critical operational regimes. *International Journal of Refrigeration*, 36(6):1750 – 1761, 2013.

[12] W. Chen, C. Shi, S. Zhang, H. Chen, D. Chong, and J. Yan. Theoretical analysis of ejector refrigeration system performance under overall modes. *Applied Energy*, 185:2074 – 2084, 2017. Clean, Efficient and Affordable Energy for a Sustainable Future.

[13] K. Chunnanond and S. Aphornratana. Ejectors: applications in refrigeration technology. *Renewable and Sustainable Energy Reviews*, 8(2):129 – 155, 2004.

[14] K. Cizungu, M. Groll, and Z. Ling. Modelling and optimization of two-phase ejectors for cooling systems. *Applied Thermal Engineering*, 25(13):1979 – 1994, 2005.

[15] J. G. del Valle], J. S. Jabardo], F. C. Ruiz], and J. S. J. Alonso]. An experimental investigation of a r-134a ejector refrigeration system. *International Journal of Refrigeration*, 46:105 – 113, 2014.

[16] I. Eames, S. Aphornratana, and H. Haider. A theoretical and experimental study of a small-scale steam jet refrigerator. *International Journal of Refrigeration*, 18(6):378 – 386, 1995.

[17] J. Fabri and R. Siestrunck. Supersonic air ejectors. volume 5 of *Advances in Applied Mechanics*, pages 1 – 34. Elsevier, 1958.

[18] A. Hakkaki-Fard, Z. Aidoun, and M. Ouzzane. A computational methodology for ejector design and performance maximisation. *Energy Conversion and Management*, 105:1291 – 1302, 2015.

[19] S. He, Y. Li, and R. Wang. Progress of mathematical modeling on ejectors. *Renewable and Sustainable Energy Reviews*, 13(8):1760 – 1780, 2009.

[20] B. Huang, J. Chang, C. Wang, and V. Petrenko. A 1-d analysis of ejector performance. *International Journal of Refrigeration*, 22(5):354 – 364, 1999.

[21] O. Ipakchi, A. Mosaffa, and L. G. Farshi. Ejector based co2 transcritical combined cooling and power system utilizing waste heat recovery: A thermoeconomic assessment. *Energy Conversion and Management*, 186:462 – 472, 2019.

[22] J. H. KEENAN. An investigation of ejector design by analysis and experiment. *Journal of Applied Mechanics*, 17:299, 1950.

[23] O. Lamberts. *Choking and mixing phenomena in supersonic ejectors*. PhD thesis, Université Catholique de Louvain, 2018.

[24] O. Lamberts, P. Chatelain, and Y. Bartosiewicz. Numerical and experimental evidence of the fabri-choking in a supersonic ejector. *International Journal of Heat and Fluid Flow*, 69:194 – 209, 2018.

[25] O. Lamberts, P. Chatelain, N. Bourgeois, and Y. Bartosiewicz. The compound-choking theory as an explanation of the entrainment limitation in supersonic ejectors. *Energy*, 158:524 – 536, 2018.

[26] J. Liu, L. Wang, L. Jia, and H. Xue. Thermodynamic analysis of the steam ejector for desalination applications. *Applied Thermal Engineering*, 159:113883, 2019.

[27] K. MATSUO, K. SASAGUCHI, Y. KIYOTOKI, and H. MOCHIZUKI. Investigation of supersonic air ejectors : Part 2, effects of throat-area-ratio on ejector performance. *Bulletin of JSME*, 25(210):1898–1905, 1982.

[28] J. T. Munday and D. F. Bagster. A new ejector theory applied to steam jet refrigeration. *Industrial & Engineering Chemistry Process Design and Development*, 16(4):442–449, 1977.

[29] S. C. Perez and Y. Fang. Private communication.

[30] M. Rahamathullah, K. Palani, T. Aridass, P. Venkatakrishnan, Sathiamourthy, and S. Palani. A review on historical and present developments in ejector systems. *International Journal of Enginnering Research and Applications*, pages 10–34, 03 2012.

[31] E. Rogdakis and G. Alexis. Design and parametric investigation of an ejector in an air-conditioning system. *Applied Thermal Engineering*, 20(2):213 – 226, 2000.

[32] A. Selvaraju and A. Mani. Analysis of an ejector with environment friendly refrigerants. *Applied Thermal Engineering*, 24(5):827 – 838, 2004.

[33] S. Sherif, W. Lear, J. Steadham, P. Hunt, and J. Holladay. Analysis and modeling of a two-phase jet pump of a thermal management system for aerospace applications. *International Journal of Mechanical Sciences*, 42(2):185 – 198, 2000.

[34] L. Shi, G. Zhao, Y. Yang, D. Gao, F. Qin, X. Wei, and G. He. Research progress on ejector mode of rocket-based combined-cycle engines. *Progress in Aerospace Sciences*, 107:30 – 62, 2019.

[35] S. T. Taleghani], M. Sorin, and S. Poncet. Modeling of two-phase transcritical co2 ejectors for on-design and off-design conditions. *International Journal of Refrigeration*, 87:91 – 105, 2018.

[36] B. M. Tashtoush, M. A. Al-Nimr, and M. A. Khasawneh. A comprehensive review of ejector design, performance, and applications. *Applied Energy*, 240:138 – 172, 2019.

UNIVERSITÉ CATHOLIQUE DE LOUVAIN
École polytechnique de Louvain
Rue Archimède, 1 bte L6.11.01, 1348 Louvain-la-Neuve, Belgique | **www.uclouvain.be/epl**